Title

On the remarkable fracture toughness of 90 to 97W-NiFe alloys revealing powerful new ductile phase toughening mechanisms

Authors

Alam, ME
Odette, GR

Publication Date

2020-03-01

DOI

10.1016/j.actamat.2020.01.012

Peer reviewed

On the Remarkable Fracture Toughness of 90 to 97W-NiFe Alloys Revealing Powerful New Ductile Phase Toughening Mechanisms

M. E. Alam, G. R. Odette*

Materials Department, University of California, Santa Barbara, CA 93106, USA

alam@engineering.ucsb.edu (M.E. Alam), odette@engineering.ucsb.edu (G.R. Odette)

*Corresponding author. Tel.: +1 (805) 964-5586; fax +1 (805) 893-8651

Abstract

Tungsten is generally too brittle to serve a robust structural function. Here, we explore the fracture toughness of 90 to 97 wt.%W Fe-Ni liquid phase sintered tungsten heavy alloys (WHAs). The room temperature (RT) maximum load fracture toughness (K_{Jm} ≈ 69 to 107 MPa√m) of the WHA, containing only 3 to 10 wt.% of a Ni-Fe ductile phase (DP), is ≈ 9 to 13 times higher than K_{Ic} typical of monolithic W (≈ 8 MPa√m). All the WHAs show extensive stable crack growth, and increasing blunting line toughness averaging ≈ 170 MPa√m, prior to significant crack extension. In contrast to classical ductile phase toughening, that is primarily due to macrocrack bridging, the WHA toughness increase mainly involves new mechanisms associated with arrest, blunting and bridging of numerous dilatational shielding process zone microcracks in the macrocrack process zone. Tests down to -196°C, to partially emulate irradiation hardening, show decreasing toughness and a transition to elastic fracture at a temperature of -150°C for 90W to -25ºC for 97W. However, even at -196°C, the leanest DP 97W WHA K_{Ic} is ≈ 3 times that of monolithic W at RT. Possible effects of the small specimen size used in this study are briefly summarized.

Keywords: Tungsten heavy alloy; liquid phase sintered WNiFe; tensile; fracture toughness; ductile phase toughening.

1. Introduction

Due to its high melting temperature, good thermal conductivity, low sputtering rates and high strength, tungsten (W) is currently considered to be the most promising candidate for plasma facing components of the fusion reactor divertor applications [1–4]. However, elevated brittle to ductile transition temperatures and low toughness combined with low tensile ductility, which are further degraded in service by neutron irradiation, limit the application of monolithic W as a structural material [1–7]. There have been many attempts to improve the ductility and toughness of tungsten by alloying, grain refining-nanostructuring and compositing [1–3,5–17]. For example, Re is known to improve the ductility of W by solid solution softening that enhances dislocation mobility, and increasing the number of available slip systems [1,12–16]. However, the use of Re in W may be impractical due to its cost and detrimental effect on radiation damage [1,18]. Other solutes, like Ta, V, Mo, Os, Ti and Cr, generally have negligible to negative effects on W ductilization [1,15–17]. Grain refinement by rolling, severe plastic deformation (SPD), and oxide dispersion stabilization, generally improves W ductility to some extent, but has mixed effects on toughness [6–9,19]. However, such deformation processing paths result in highly anisotropic properties and textured microstructures, and are otherwise likely unsuitable for fabricating complex components [1,6–10].

One promising approach to toughening is to composite W with a ductile phase. Ductile phase toughening (DPT) restricts crack propagation in brittle matrix systems by crack bridging, arrest/re-nucleation and deflection mechanisms. Indeed DPT has been successfully applied in many brittle matrix systems [20–23]. Tungsten heavy (metal) alloys (WHAs), or composites, typically containing 78-98 wt.% W, along with a balance

of ductile phase metals like Ni, Fe, Cu, Co, have been studied for several decades [24–40]. The WHAs are typically composed of W powders consolidated by liquid phase sintering (LPS). Most of the previous research focused on processing optimization and relating WHA microstructures to their tensile properties. WHAs are used in radiation shields, kinetic energy penetrators, counterbalances, vibration dampers, and rocket nozzles. A good review paper on WHAs can be found in [41].

Recently, various WHAs have been considered as potential structural plasma facing materials for fusion reactor divertor applications [5,28,42,43]. Important characteristics of the WHA ductile phase constituent include:

Melting temperature (T_m)

Strength, ductility and toughness

Immiscibility with W and the absence of brittle intermetallic phase formation

The W-ductile phase interface bond strength

Long half-life radioactivity of ductile phase constituents.

For example, W-Cu WHAs have been extensively studied, but suffer both from a Cu $T_m \approx 1085$ºC, and strength that are both low compared to the 50Ni30W20Fe face centered cubic solid solution phase that forms during the LPS of the W powders studied in this work. The $T_m \approx 1450$ºC of the NiWFe phase [44] is comfortably above the 1300°C limit, typically imposed on divertor applications of monolithic W, in order to avoid highly embrittling recrystallization [42,43]. Further, W-based divertor components will almost certainly be metallic hybrid systems; for example, the WHA may serve as a crack arrest layer for He-cooled plasma facing thimbles composed of bonded multilayers, like W-WHA-oxide dispersion strengthened (ODS) steels-Cu alloys [1–3].

WHAs generally have fairly good room to high-temperature tensile strength and ductility [28–31,34–36,39–41]. However, the key limiting structural property for W and W-alloys is usually fracture toughness and a high brittle to ductile transition temperature (BDTT) [3,6–8]. It is important to emphasize that fracture toughness relates to the resistance of a material to the propagation of a pre-existing sharp crack. Thus, fracture toughness cannot be determined by the strength and ductility as measured in tensile or flexure tests. Indeed, a metal may be ductile in a tensile test, while being extremely brittle in a fracture toughness test. Low fracture toughness is a significant issue for fusion divertor applications, since high and cyclic thermal loads typically result in the formation of many sharp surface cracks [1,2,11,45].

There are very few papers in the literature reporting pre-cracked fracture toughness data on W-NiFe WHAs. The most useful study reported RT resistance curve J-da R-curve data for ≈ 93-95W WHAs [37]. The ASTM E813-88 based initiation K_{Jc} ranged from 152 to 210 MPa√m. Strong resistance curve behavior was observed along with extensive stable crack growth in small 3PB specimens (thickness B ≈ 4.5 to 6.5 mm).

The objective of this study is to measure the fracture toughness, and to explore the toughening mechanisms, in four 90 to 97W-NiFe WHAs from RT down to liquid nitrogen temperature (-196°C), using fatigue precracked bend bars following ASTM test standards discussed below [46]. The lower temperature tests were intended to partially emulate the irradiation hardening that occurs at higher temperatures in service. Microhardness and uniaxial tensile tests from -196°C to RT were also conducted. Optical

and scanning electron microscopy (SEM) were used for microstructural characterization and to investigate the fracture mechanisms and modes.

The W-NiFe WHA microstructure is composed of a 3-dimensional, NiWFe ductile phase honeycomb web surrounding the unalloyed W powders. Our study revealed that the toughening in the W-NiFe WHA is dominated by new mechanisms associated with this microstructure. In most classical ductile phase toughening systems, the matrix phase remains brittle, while the ductile phase toughening is due to bridging of the *macrocrack* wake, as well as crack arrest-re-nucleation-deflection mechanisms [20,22]. However, in the case of the W-NiFe WHA, toughening is dominated by *microcrack* arrest, blunting and bridging in a fully ductilized crack tip plastic zone. Plastic zone deformation, including in the embedded W particles themselves, and dilatational microcrack blunting, dissipate large amounts of energy. Further, the process-zone dilatation extensively shields the crack tip stress fields, including wake effects. Plastic microcrack blunting shielding is far more effective than that provided by elastic microcracks in brittle matrix systems [47–49]. To the best of our knowledge, these *ductile* process zone microcrack toughening mechanisms have not previously been identified and explored in metallic alloys. However, similar toughening effects have been observed in some polymer-rubber composites [50].

The small pre-cracked bend bar specimens used in this study might raise issues of possible size and geometry effects on the measured fracture toughness and stable crack growth characteristics of these WHAs. This issue has been explored in some detail, but is beyond the scope of this paper. Hence, these results are only briefly summarized in the Results Section 3.3.

2. Materials and Methods

2.1 Materials

The four commercial (Mi-Tech Metals, Indianapolis, IN, USA) liquid-phase sintered (LPS) were received in the form of 100mm x 100mm x 14mm plates. The WHAs contained 90, 92.5, 95 and 97 wt. % W, as shown in Table 1, with a balance of an initially 70% Ni and 30 %Fe phase. The Ni-Fe phase is enriched with 30%W during LPS resulting in an fcc solid solution composition of ~ 50% Ni, 30% W and 20% Fe, which we call the NiWFe ductile phase (DP). The NiWFe phase forms a semi-continuous honeycomb web structure surrounding a much larger volume fraction of W-particles.

Table 1. WNiFe alloy compositions (wt.%) and the size and contiguity of the W particles

WHA	W	Ni	Fe	W particle size (μm)	W-W contiguity, C_w
90W	90.27	6.78	2.95	17 ± 7	0.161
92.5W	92.48	5.33	2.19	18 ± 7	0.197
95W	95.03	3.48	1.49	26 ± 11	0.224
97W	97.13	2.01	0.86	38 ± 15	0.315

2.2 Microstructural characterization

The WHA specimens (see below) were fabricated by electrical discharge machining (EDM). They were ground with 220 to 2000 grit sand paper to remove EDM damage and residual surface stresses. Some specimens were then polished down with 0.5μ-diamond paste and etched in a 30% hydrogen peroxide solution for 10 min to facilitate microstructural characterization. Scanning electron microscopy (SEM) with energy dispersive spectroscopy (EDS), and electron backscatter diffraction (EBSD) were used to image the W particles and the surrounding NiWFe ductile phase, and to identify

their respective compositions. The W particle size distribution was determined by sampling ~500 individual W powder particles using 'ImageJ64' software. The particle aspect ratio (PAR) was defined by dividing the longest dimension (l) to the shortest dimension (s) of a particle. The cleavage crack length and the mid-crack opening displacement were defined by measuring the length and the maximum width of a crack, respectively. Contiguity (C_w) defines the amount of W-W contact, and is expressed as $C_w = (S_{w-w})/S_w$ where S_w is the surface area of the W grains, and S_{w-w} is the surface area of W-W contacts [34,35]. The area fraction of the NiWFe was determined by converting SEM EBSC micrographs into binary black-white images, and measuring the fraction of the white area (see Fig. 1). The NiWFe DP honeycomb structure thickness (t) was measured using a line-intercept method (LIM), as the average width of the NiWFe phase measured on lines drawn on the binary image [30]. The NiWFe DP thickness/W length ratio was also calculated by the same LIM, by dividing the total intersected DP length by the total intersected W length. The percentages of the various local fracture modes were also determined by the LIM.

2.3 Microhardness and tensile testing

Vickers microhardness measurements (H_v) at RT were performed on the polished surfaces at a 500g load with 10 seconds dwell, using a LECO M-400A semi-automated hardness tester. The reported average values and standard deviations are based on 10 to 15 indents. A Zwick microhardness tester was used for corresponding H_v measurements at the liquid nitrogen (LN_2) boiling point of -196°C, also at a 500g load. In this case, polished hardness specimens were located inside a small insulated stainless-steel cup mounted on a stage below the indenter. A charge of LN_2 was poured into the cup to cool

the specimen and indenter that were held for 5 minutes to reach a stable temperature of ≈ -196°C.

Uniaxial tensile tests from RT to -196°C were performed on EDM fabricated flat dog-bone shaped sub-sized SSJ-2 specimens with a gauge section length x width x thickness of 5.0 x 1.2 x 0.5 mm [51]. The tensile specimens were sanded with 1500 grit to remove surface oxides and contamination, minor cracks and local residual stresses due to the electrical discharge machining (EDM). Tests were carried out on a MTS 810 servo-hydraulic universal testing machine, equipped with a LN_2 cooling chamber. A controlled LN_2-air mixture was injected into the cooling chamber to reach the targeted temperature that was stabilized for 30 to 45 min before testing. The tensile tests were conducted at a displacement rate of 0.30 mm/min, equivalent to a strain rate ≈ 10^{-3}/s; at least 3 tests were conducted for each alloy-temperature condition. The tensile properties were generally determined in accordance with ASTM test standard E8M-15a [52]. The strain hardening exponent (n) was determined by fitting a simple power-law hardening equation

$$\sigma_t = k\varepsilon_t^n,$$

where σ_t and ε_t are the true stress and true strain from yielding to the onset of necking (e.g., the plastic portion of true stress-strain), and k is strength coefficient.

2.4 Fracture toughness tests

Room temperature fracture toughness tests were primarily conducted on small fatigue pre-cracked, single-edge notch bend bar specimens with a nominal length (L) x width (W) x thickness (B) dimensions of 16 x 3.3 x 1.65 mm [53]. The specimens were pre-cracked to nominal crack length (a)-to width (W) ratios, (a/W) ≈ 0.40 to 0.5 up to a maximum ΔK_I =18 MPa$\sqrt{m}$ and a load ratio R = 0.1. The specimens were heat-tinted at

400ºC for 1 min to mark the pre-crack front. Both three-point (3PB) and four-point (4PB) bend fixtures were used on a 810 MTS servo-hydraulic universal testing machine. To facilitate *in-situ* optical observation of the crack tip region, the fracture specimen sides were sanded with a sequence of 2000 grit SiC followed by 9µ, 3µ and 1µ diamond lapping paper. Initially 4PB tests were conducted at RT, in part to permit extensive crack growth without the influence of the loading tup. However, since the crack growth was generally found to be highly stable, subsequent fracture tests used a 3PB fixture with only limited crack growth.

The fracture tests were carried out at a crosshead speed of 0.04mm/min. ASTM standards E1921 [46] and ASTM C1421 [54] were used to calculate the elastic components of the fracture toughness, for the 3PB and 4PB tests, respectively. ASTM E1921 was used to calculate the plastic component for the both 3PB and 4PB tests. The K_{Jm} were calculated at the maximum load (P_m) in the load-displacement (P-d) curve. Blunting curve toughness ($K_{J0.8}$) was also evaluated at post-peak loads down to ≈ 80% of P_m, since there was minimal crack growth (< 200 µm) for the displacements up to this loading point. The 4PB tests were carried out down to very low P, resulting in extensive crack tearing to near the back of the specimen. The 3PB tests were stopped at P/P_m of 0.77 to 0.92 to better evaluate an initiation toughness and corresponding crack tip opening displacement (CTOD) which ranged from 16 to 56 µm, averaging 35 ± 13 µm. The pre-crack and post-test crack lengths were also measured after the specimens were broken in LN_2 to ensure no further ductile crack extension had occurred. All the low-temperature toughness tests were conducted using 3PB fixture as described in [53], and P_m was used to calculate K_{Jm}. Three to seven specimens were tested for each condition.

3. Results

3.1 Microstructural characterization

The SEM micrographs of the polished and etched W-NiFe plates shown in Fig. 1 reveal roughly spheroidal W particles (PAR: 1.1 ± 0.2) surrounded by an interconnected honeycomb web structure of the ductile NiWFe phase. As summarized in Fig. 1 and Table 2, multiple EDS and electron probe microanalysis (EPMA) scans show that the particles are close to 100% W (point 1 of Fig. 1g), while the NiWFe ductile phase is approximately 50%Ni, 30%W and 20%Fe, by wt.% (point 2 of Fig. 1g). Figure 1 and Table 1 also shows that the W–particle size increases from ≈ 17 μm for 90W alloy to ≈ 38 μm for 97W alloy. The increase in the particle size with increasing particle loading is associated with less dissolution of W needed to maintain a similar composition in the NiWFe phase. The average NiWFe web thickness is roughly similar in all the W-NiFe WHAs at ≈ 4.9 ± 0.8 μm. As expected, the area fraction of the NiWFe phase decreases from ~16% for 90W to ~6% for 97W. However, significant microstructural inhomogeniety was observed for different plates of same WHA, as well as within the same plate. For example, the average local DP area fraction for two specimens, from the same 90W plate, ranged from 22.4 and 13.1%; in the case of the 97W specimens the corresponding values ranged from 9.2% and 5.7% [55]. A higher W fraction lowers the NiWFe phase continuity and increases both the W-W contiguity and the frequency of particle bonded W-W interfaces [35], accompanied by a lower NiWFe t/W ratio (Fig. 1e,f and Tables 1 and 2). Fig. 1c shows the 95W WHA contains some pre-test cracked W particles (also, see the red short arrows in Fig. 1g), although the reason for this is not known. The EBSD inverse pole figure (IPF) maps (not shown) confirm expected random

orientations of the W particles. Some large particles show multiple orientations, due to internal grains or subgrains. These collective observations may be important considerations in tailoring the design of WHA.

Table 2. The composition and morphology of the NiWFe honeycomb web structure

WHA	Ni/W/Fe (wt.%)	NiWFe Area fraction (%)	Thickness, t (μm)	t/W (μm/μm)
90W	51.2/28.5/20.3	16.1 ± 3.8	5.9 ± 5.4	0.22
92.5W	49.1/31.3/19.6	11.8 ± 2.2	4.0 ± 3.7	0.12
95W	49.1/32.2/18.7	10.7 ± 1.3	5.1 ± 4.1	0.13
97W	48.3/34.3/17.4	6.4 ± 1.5	4.5 ± 5.0	0.07

t = NiWFe thickness, W = tungsten fraction

3.2 Microhardness and tensile tests

Vicker's microhardness (H_v) results for W-alloys tested at RT and -196°C are shown in Fig. 2(a). The average hardness increases with increasing W at both RT (slightly) and -196°C (more strongly). As expected, the H_v is substantially higher at -196°C (507 ± 7 kg/mm^2 for 90W and 609 ± 21 kg/mm^2 for 97W) than at RT (321 ± 9 kg/mm^2 for 90W and 344 ± 9 kg/mm^2 for 97W). Monolithic W was also tested both at 23ºC (RT) and -196 °C, exhibiting a H_v of 358 ± 39 and 686 ± 79 kg/mm^2, respectively. No indentation cracking was observed in any of the alloy-test conditions.

Fig. 2(b) shows the engineering stress-strain $\sigma(\varepsilon)$ curves for all the WHA alloys tested at room temperature and -196ºC, along with a typical RT reactor pressure vessel (RPV) steel ($\sigma_y \approx 600$ MPa) for comparison. The corresponding tensile data is shown in

Table 3, including for tests at -100°C. The RT $\sigma(\varepsilon)$ curves are generally similar, although the total elongation systematically decreases with increasing W. Significant strain hardening is observed in all cases at RT (see Table 3). The σ_y decreases above 95W at -100°C and above 90W at -196°C (see Table 3 and Fig. 2c). In these cases, the tensile fracture is elastic with $\varepsilon_t = 0$, and at a fracture stress less than σ_y. Note that the microhardness increases with increasing W, especially at low temperatures, since loading is primarily in compression rather than tension.

Table 3. Tensile properties of W-NiFe WHAs as a function of W content and temperature

T (°C)	WHAs	σ_y (σ_f) (MPa)	σ_u (MPa)	ε_u (%)	ε_t (%)	n
23	90W	621 ± 29	891± 35	18 ± 4	21 ± 7	0.23 ± 0.01
	92.5W	616 ± 44	886 ±12	13.5 ± 2.2	16 ± 4	0.23 ± 0.02
	95W	600 ± 15	818 ± 10	7.3 ± 1	8 ± 1	0.22 ± 0.02
	97W	594 ± 27	701 ± 67	3.4 ± 1	4 ± 1	0.16 ± 0.06
-100	90W	978 ± 16	1162 ± 20	7.5 ± 0.4	7.7 ± 0.4	0.16 ± 0.01
	92.5W	989 ± 28	1149 ± 16	4.0 ± 0.7	4.2 ± 0.7	0.15 ± 0.01
	95W	1019 ± 18	1019 ± 18	0	0	-
	97W	673 ± 101	673 ± 101	0.0	0.0	-
-196	90W	1292 ± 59	1332 ± 16	0.2 ± 0.4	0.2 ± 0.4	-
	92.5W	1151 ± 46	1151 ± 46	0	0	-
	95W	673 ± 48	673 ± 48	0	0	-
	97W	563 ± 31	563 ± 31	0	0	-

σ_y = 0.2% yield stress, σ_f = fracture stress, σ_u = ultimate tensile strength, ε_u = uniform elongation, ε_t = total elongation, n = hardening exponent.

Fig. 2(d) shows the total elongation (ε_t) decreases with increasing W at RT. The ε_t also decreases with decreasing temperature, falling from ≈ 21% to ≈ 8% for 90W and ≈

16% to ≈ 4% for 92.5W at RT and -100ºC, respectively. Moreover, ε_t ≈ 0% at -196ºC for all W contents (see Table 3). The 95W to 97W also fall to 0% (elastic fracture) at -100ºC. The uniform elongation (ε_u) is very close to ε_t, since fracture takes place almost immediately after the onset of necking, except for 90W and 92.5W RT tests with the reductions of area (RA) varying between ≈ 27 to 13%, respectively.

SEM micrographs of the fracture surfaces of the broken RT tensile WNiFe specimens, shown in Fig. 3, manifest four local failure modes, namely: W-W interparticle fracture (WW), W cleavage (WC), W-NiWFe interfacial debonding (WD), and NiWFe ductile phase rupture (DR). These local failure modes have been widely reported in previous studies of WHA [24,29,30,33–35,37–40]. The WW interface is the weakest and, as expected, this fracture mode increases with increasing W [24,29,34,35,37–40]. More quantitatively, WW fracture correlates with the fraction of contiguity (C_w), which also increases with increasing W% (see Table 1). Global fracture often initiates at W-W fracture sites and continues by cleavage crack propagation through the W particles, leaving intact NiWFe web ligaments that can arrest the microcracks. Figs. 3(a)-3(d) show that the fraction of WC is highest for the 90W WHA, which experience the lowest number of WW events, and is least for the 97W alloys that experience more WW fracture. Notably, WC fracture appears to correlate with higher tensile strength and ductility (see Table 3 and Fig. 3). Ductile web knife-edge rupture features surround the fracture facets.

While at RT more WC fracture correlates with higher ductility, at lower temperatures the fracture surfaces shown in Fig. 4 indicate the opposite trend, with increasing amount of WC fracture leading to decreasing ductility. The increase in WC

with decreasing temperature is due to the corresponding decrease in the cleavage fracture toughness of the W particles. The strength and ductility of the ductile NiWFe phase is much less sensitive to temperature than the W-particle fracture stress [33]. For example, the 90W alloy shows increasing amount of WC fracture at -100ºC coupled with a lower ε_t ≈ 8% compared to 21% at RT, and an ε_t ≈ 0% at -196°C, where almost 100% WC is observed. In general, the fraction of WC increases with increasing W% and decreasing temperature, leading to lower or no ductility below RT.

3.3 Room temperature fracture toughness tests

RT fracture toughness tests were conducted on the 16 x 3.3 x 1.65 mm (nominal dimensions) single-edge notched fatigue pre-cracked bend bars using both 4PB and 3PB test fixtures. The fatigue cracks tend to mainly propagate through the NiWFe DP, irrespective of alloy compositions, as shown by the white arrows in Fig. 5a. In situ measurement of crack growth during the test (e.g. optically and by digital image correlation) proved to be difficult due to the large plastic zone and lateral contraction (the black arrows in Fig. 5b and c) near the blunting crack tip. Further, crack wake bridging precludes the use of standard unloading compliance methods to measure da. Thus K_{Jm} was defined at the maximum load (P_m) based on the ASTM E1921 standard practice method of estimating the elastic-plastic J-integral J_m, as $K_{Jm} = \sqrt{\{J_m E/(1-\nu^2)\}}$, where E is the elastic modulus (≈ 400 GPa) and ν is Poisson's ratio (≈ 0.28) [46,56]. The ASTM E1921 validity limit for the specimen dimension is given by $K_{Jlim} = [Eb_o\sigma_y/30(1-\nu^2)]^{0.5}$, where b_o is the unbroken ligament (here 1.65 to 2.00 mm), and σ_y is the yield stress at test temperature (≈ 600 MPa at 23ºC). Thus, K_{lim} is ≈ 120 to 132 MPa√m. This K_{lim} is larger than all of the measured maximum load RT initiation toughness, K_{Jm} (≈ 93 ± 19

MPa√m, see Table 4). Hence the data are, in this sense, valid since cleavage could have occurred if the lower toughness ductile tearing processes had not intervened. Note, in steels, cleavage still sometimes occurs at $K_{Jm} > K_{lim}$, beyond the validity limit and after a small amount of ductile tearing, but this did not happen in the small W-NiFe WHA specimens. Further, it was found that small subsequent decreases of P below P_m remained on the blunting line, without significant crack growth. The decrease in P is mainly due to microcracking in the process zone (Fig. 5d). Here, the microcracking is primarily transgranular W cleavage (WC), shown by the thick-red arrows in Fig. 5d. Nevertheless, the small specimen dimensions might raise a question about size effects. Therefore, we have tested from 3x to 8x larger specimens at RT. Similar toughening mechanisms (discussed below) were observed for all the larger specimens that experienced ductile tearing, which is the main focus of this paper. However, tests on 97W using specimens that were 3 times larger, experienced elastic fracture, rather than ductile tearing, at a $K_{Ic} \approx 38 \pm 4$ MPa√m; notably this is still ≈ 5 times higher than for monolithic W. In contrast, all the specimens up to 8x larger for 90W to 95W experienced ductile tearing, showing only modest effects of size. For example, K_{Jm} is 84 ± 11 and 81 ± 7 MPa√m for the 3x and 8x larger specimens, respectively, compared to 96 ± 12 MPa√m for the small 92.5W WHA. However, discussion of size and geometry effects on WHA fracture is beyond the scope of this paper. Preliminary results can be found elsewhere [55], and will be reported in a future publication.

Continued loading beyond $P = P_{0.8}$ leads to initiation of extension and stable growth of cracks in the 4PB P-d tests that were continued to very large displacements (d). Stable crack growth is reflected in the normalized load-displacement (P_n-d) curves shown

in Fig. 6a. The normalization involves adjusting the measured P for various a/W to a common P for a/W = 0.5, based on the limit load ratio, $P_n = 0.25P/(1-a/W)_2$ [56]. The peak loads are similar except for the 95W alloy where the normalized P_m is somewhat higher for this particular test (see Fig. 6b). The P-d curves have an elastic loading region, followed by a plastic yielding deviation from linearity. The subsequent increasing P is due to the growth of the plastic zone and strain hardening. The much larger decreases in P following P_m reflect stable crack growth. Since 4PB tests show massive stable crack growth, additional tests were conducted on very finely ground (down to 1μ with diamond lapping paper) specimens in 3PB fixture, and a Questar long-distance (telescopic) optical microscope with 3-axis positioning was used to observe *in-situ* crack initiation and propagation at a frame rate of 6/min, as shown in Fig. 7. Here the black curve is the P-d for 97W. The numbers 1 to 5 correspond to the optical images at the loading points. The blue squares are the corresponding K_J for corresponding red-circled P-d points.

The 3PB tests were stopped at a P/P_{max} from ≈ 0.77 to 0.92, since the lateral contraction and surface dimpling, indicated by the dark areas in Figs. 5b and 7, prevented imaging the crack tip. However, post-test optical and SEM images show that the crack extends by ≈ 130μm due to blunting at $P/P_m \approx 0.88$ with a corresponding blunting line toughness of $K_J \approx 139$ MPa√m, which is significantly higher than the maximum load K_{Jm} ≈ 80 MPa√m (see insert of Fig. 7). Pre-and post-test SEM micrographs for all the RT 3PB tests show very little crack growth (da < 200 μm) when the loading was stopped (see Fig. 5d, for example). Thus, the K_J at $P/P_m \approx 0.8$ ($K_{J0.8}$) is plotted along with K_{Jm} in Fig. 6b. These results show that the $K_{J0.8}$ is ≈ 60-85% higher than K_{Jm} for the 90W to 95W alloys and ≈ 95% higher at 97W.

The RT tensile results for the W-NiFe alloys show a systematic decrease in ultimate strength and ductility with an increasing W fraction. In contrast, the RT K_{Jm} are essentially the same up to 95W, averaging 100 ± 15 MPa√m, in spite of the contiguity increase (see Tables 1 and 4). The K_{Jm} decreases to between 95W and 97W, where K_{Jm} = 69 ± 12 MPa√m. In this case, the K_{Jm} toughness is still ≈ 9x higher than that for typical monolithic W with K_{Ic} ≈ 8 ± 4 MPa√m; the corresponding $K_{J0.8}$ = 142 ± 8 MPa√m is ≈ 18x higher. The massive toughening provided by a relatively small addition of ≈ 5 vol.% (≈ 3 wt.%) of the ductile phase is remarkable. From a practical engineering perspective, crack initiation followed by extremely stable crack growth provides very high effective cracked body ductility in all cases.

Table 4: The K_{Jm} and $K_{J0.8}$ for the W-NiFe WHAs

Temp (ºC)	K_{Jm} or K_{Ic} (MPa√m)			
	90W	92.5W	95W	97W
23	97 ± 17	96 ± 12	107 ± 14	69 ± 12
-50	-	59 ± 9	65 ± 4	40 ± 2
-100	73 ± 4	48 ± 5	35 ± 4	32 ± 0.1
-150	50 ± 1	-	-	-
-196	36 ± 3	30 ± 3	27 ± 5	25 ± 2
23ºC ($K_{J0.8}$)	176 ± 25	152 ± 22	204 ± 20	142 ± 8

Post-test SEM studies of the sides of the 3PB bars, shown in Figure 8, demonstrate some of the multiple interacting toughening mechanisms: (i) crack wake bridging; (ii) process zone microcrack and microcrack bridging; and, (iii) as indicated by slip lines (and the grain shape changes, white dashed circles, as noted previously), plastic

deformation of otherwise brittle W particles encapsulated by the DP. These mechanisms lead to the ductilization of the entire W-NiFe dual phase microstructure resulting in large crack tip CTOD ductility and the corresponding development of large semi-classical plasticity zones. That is, on a macro scale, the RT fracture of the small W-NiFe WHA bend bars is entirely ductile.

All four types of local fracture modes (WC, WD, WW, DR) for the RT tensile tests reported in the literature [19,29,37,39] are similar to those observed in our RT toughness tests, as seen in Fig. 8d. As shown in Table 5, the fraction of WW increases and WD decreases systematically with increasing W, and the two modes account for ≈ 80% of the total local fracture. Side surface observations (Figs. 5d, and 8b) clearly show that there are large numbers of WC microcracks in the process zone that blunt and open under increasing load, thus producing large dilatational shielding effects.

3.4 Lower temperature fracture toughness

Precracked 3PB were carried out on the W-NiFe WHAs at -50, -100, -150 and -196°C. The objective of these tests was to probe the effects of lower W toughness, associated with a higher $\sigma_y(T)$, to at least partly emulate the effects of irradiation hardening. Figure 9 shows representative normalized load-displacement (P-d) curves for all four W-NiFe WHAs from 23°C to -196 ºC. Table 4 summarizes the corresponding K_{Jm}. Three to four tests were conducted for each condition (all the normalized P-d curves can be found in [57]). Note that, with only a few exceptions, the normalized peak loads for the redundant tests are similar. Unlike at RT, with substantial plastic yielding, the lower temperature P-d curves have a distinctly different shape. They either show a sharp peak followed by stable crack growth at a rapidly decreasing P, or elastic fracture

associated with a large pop-in event. The overall average P_m at lower temperature decreases somewhat with increasing W. At -196°C elastic fracture occurs in all cases.

Table 5: The percentage of local fracture modes from toughness fractographs.

T (ºC)	Alloys	WW	WC	WD	DR
23	90W	31.7	12.0	44.1	12.2
	92.5W	37.1	10.9	40.5	11.5
	95W	42.6	13.5	32.8	11.1
	97W	67.2	17.6	10.8	4.4
-100	90W	32.6	15.5	42.4	9.5
	92.5W	15.3	68.2	13.9	2.6
	95W	2.5	91.5	5.1	0.8
	97W	4	96	0	0
-196	90W	2.6	95.6	0	1.8
	92.5W	3.7	96.3	0	0
	95W	2.7	97.3	0	0
	97W	3.5	96.5	0	0

As shown in Fig. 9a, all the 90W WHA experience stable crack growth down to -100ºC. One of three tested 90W WHA fails elastically at -150°C. Thus, the elastic transition for the 90W WHA is estimated to be ≈ -150ºC, at an average $K_{Jm} \approx 50 \pm 10$ MPa√m. All the 92.5W specimens tested at -50ºC show stable ductile tearing with K_{Jm} averaging ≈ 59 ± 9 MPa√m (see Table 4 and Fig. 9b). However, only one of three 92.5W WHA tested at -100ºC experienced stable ductile tearing, while the others fracture elastically. Thus, the estimated elastic transition for the 92.5W WHA is ≈ -100ºC, with an

average K_{Jm} value ≈ 48 ± 5 MPa√m. Similar to 92.5W alloy, 95W alloy also shows stable crack growth at -50ºC (see Fig. 9c). However, all the specimens tested at -100ºC and -196ºC show only elastic fracture. Thus, the corresponding BDT temperature of 95W WHA is estimated to be -75ºC with K_{Jm} ≈ 50 ± 15 MPa√m. Only one 97W WHA test showed stable crack growth at -50ºC, while others at -50ºC and lower temperatures experience elastic fracture (Fig. 9d). Therefore, a reasonable estimate of the BDT for 97W indexed at K_{Jm} = 50 MPa√m is ≈ -25ºC.

The corresponding K_{Jm} values are plotted in Fig. 10 and summarized in Table 4, respectively. The RT K_{Jm} is nearly constant up to 95W, but lower temperature K_{Jm} shows a noticeable decrease with increasing W and decreasing temperature. All the WHAs tested at -196°C fracture elastically with similar $K_{Jm} = K_{Ic}$ ≈ 31 ± 6 MPa√m. Note there is no difference between K_{Jm} and K_{Ic} for fully elastic fracture. However, the average WHA K_{Ic} at -196°C is still much higher than that at RT for monolithic W with a K_{Ic} ≈ 8 ± 4 MPa√m, as shown in Fig. 10a. In general, in contrast to tensile strength, the K_{Jm} and K_{Ic} decrease with decreasing temperature and increasing tensile strength.

The plastic zone sizes at P_m decrease with decreasing temperature reflecting the higher σ_y. Representative SEM fractographs for 90W and 97W at varying test temperatures are shown in Fig. 11a and b, respectively. The percentages of the various local fracture modes are summarized in Table 5 and the averages as a function of temperature are shown in Fig. 10d along with the average K_{Jm}. The LIM analysis shows that the fracture surface at RT is dominated by tungsten-tungsten interparticle boundary separation (WW) and tungsten-NiWFe ductile phase decohesion (WD), with relatively small percentage of W-cleavage (WC), or NiWFe ductile ligament rupture (DR). Since

the W K_{Ic} deceases at lower temperature, the fraction of WC increases with increasing W and decreasing temperature. The local fracture mode is ≈100% WC at -196°C in all the WHAs. In general, WC increases with increasing W, decreasing temperature (except for the 90W WHA at -100ºC, which experiences a roughly equal frequency of the 4 local fracture modes at RT) and toughness.

4. Damage Development

4.1 Tensile test damage development

Side surface SEM observations of a 90W RT tensile specimen near the necked and fractured zone in Fig. 12(a) show debonding between W particles and NiWFe ductile phase (WD, white circles). This is consistent with a FEM analysis reported by Gong *et al.* [29] that shows the maximum stresses occur at the W-ductile phase (DP) interface, assuming W particles only elastically deform while the DP is subjected to isotropic hardening under a near-hydrostatic stress state during plastic deformation. Note, however, while they are strong, the W particles can also deform plastically and elongate in the loading direction when surrounded by the softer DP, as shown in Fig. 12a for the 90W WHA, and also reported in [34]. The average deformed W particle aspect ratio (PAR) along the loading direction (parallel to the marker bar, Fig. 12) increases to ≈ 1.6 ± 0.4 from a randomly oriented value of 1.1 ± 0.2 for undeformed W. Small pores, that form at the W-NiWFe interface, increase in size with loading (small and large white circles in Fig. 12a). Larger DP ligaments remain intact and arrest the microcracks (red box in Fig. 12a, also see bottom row images). WW cleavage cracks are also arrested by the DP ligaments. Isolated W particle-sized cleavage cracks are oriented over a range of

angles with respect to the loading direction, presumably due to the combination of the result of Mode-I stress and the cleavage planes. Limited WW interface fracture is also observed (dashed arrows in Fig. 12a). Higher W% decreases the fraction of W particles that are completely surrounded by the DP, hence, they are less deformed (PAR ≈ 1.25 ± 0.2), as shown in Fig. 12b for the 97W WHA. W particle-sized WC microcracks, that interconnect to span several particles and WW interface fracture increase with W especially at 97W. This damage is responsible for the lower RT ductility in the higher W WHAs. Most previous studies reported that more frequent WC microcracks increase tensile ductility [30,34]. However, WC decreases ductility at high W due to the linking of particle-sized microcracks to form a larger, unstably growing crack. In contrast to the sharp WC microcracks at 97W, (Fig. 12b, $\varepsilon_t \approx 4\%$), widely dispersed, particle-sized and highly blunted WC microcracks increase tensile ductility (Fig. 12a, $\varepsilon_t \approx 21\%$).

The W particles that are far from the fracture zone deform only slightly at RT in the 90W WHA and do not deform at 97W WHA. Corresponding fractographs for the low temperature tensile tests show no arrested-blunted microcracks in all the WHA tested at -196 ºC (Fig. 12c,d) and in all the WHA with > 90W at -100ºC. Again, this is due to the rapid propagation of larger, interconnected, unarrested and largely unblunted microcracks following initiation in one grain and linking with other microcracks in adjacent grains. While WC is more frequent at lower temperatures, the propagation of the initial sharp, multi-particle crack leaves behind a population of sharp, single particle microcracks, and reduces the tensile ductility, in the limit leading to elastic fracture.

4.2 Fracture test damage development

Side surface observations for all room temperature toughness specimens show

large numbers of particle-sized WC blunted microcracks in the process-zone with a density of ≈ 556 (90W) to 231 (97W) per mm^2 (see Table 6 and Fig. 13 a,b). Some WW interface fracture and W-NiWFe interfacial debonding (WD) events are also observed. The WC microcracks might have initiated at small pores in the as-received WHA. The microcracks are arrested by the NiWFe DP and blunt under increased loading. The mid-crack opening displacements range from 0.3 to 15μm, averaging from 1.7 to 3.3μm (see Table 6). However, a few microcracks are linked up to 2 to 3 particle diameters, especially in the 97W WHA due to low amount of DP. Like in the tensile tests, both cleaved and unbroken W particles also deform along the principal stress direction. The strain in W particles normal to the loading direction, including the blunted microcracks, is again higher in the 90W WHA (≈ 0.18) compared to that in 97W WHA (≈ 0.11) (see Table 6). The small boxed areas in Fig. 14a and b show the undeformed and deformed regions at the crack tips (arrows), respectively, for the same location in a 95W WHA. The NiWFe honeycomb web is also strained normal to the loading direction (≈ 0.18 - 0.27) in all cases (DP strain in Table 6). The WHA crack tip region also undergoes lateral contraction in the thickness (Z) direction. The $\Delta Z/Z$ was measured on the broken specimens (see Fig 5(c), for example), and verified by 3D tomography using a Keyence VHX-5000 Microscope, as shown in the insert in Figure 14(c); $\Delta Z/Z \approx 0.044 \pm 0.004$ for 90-95W and ≈ 0.023 for 97W (Table 6). Fig. 14(d) schematically illustrates the deformation and dilatational damage mechanisms in the crack tip process zone.

Table 6 Process zone damage statistics of WHAs

WHA	Crack mouth opening (μm), Range (μm)	Crack length (μm)	Crack density (mm^{-2})	Process zone W strain (μm/μm)	DP strain (μm/μm)	ΔZ/Z	ΔV/V
90W (RT)	2.53 ± 1.82 (0.415 – 12.12)	15 ± 8	556	0.18	0.20	0.048	0.10
92.5W (RT)	1.66 ± 1.29 (0.270-7.431)	14 ± 6	387	0.17	0.23	0.044	0.09
95W (RT)	3.26 ± 2.63 (0.401 – 14.66)	33 ± 15	339	0.13	0.27	0.041	0.13
97W (RT)	2.28 ± 1.96 (3.47 – 11.69)	45 ± 19	231	0.11	0.18	0.023	0.05
90W (-100C)	1.42 ± 0.86 (0.270-5.763)	16 ± 9	376	0.09	0.17	0.039	0.07
97W (-100C)	0.27	49	4	0.00	0.01	0.00	0.00

ΔZ/Z = change in thickness/initial thickness, ΔV/V = change in volume/initial volume.

Unlike room temperature cracks that are more frequently aligned ~ 45º to the loading direction, the lower temperature cracks are narrow and sharp and primarily aligned perpendicular to the loading direction. In this case, once initiated, adjacent microcracks link and propagate at a much lower toughness (see Table 4 and Fig. 13 c, d). In summary, the WC and WW microcracks are arrested by DP and blunt with increasing loading. The corresponding dilatation decreases with increasing W and decreasing temperature.

5. Discussion

The microcrack arrest and blunting mechanisms, that derive from only small amounts of the ductile NiWFe phase, lead to a remarkable W-NiFe WHA ductilization and toughening. The multi-mechanism toughening will be modeled in the future, but this

is beyond the scope of the current paper. Briefly, however, as a result of the requisite 3-dimensional flow geometry of the NiWFe honeycomb web surrounding a large volume fraction of harder W particles, deformation results in a highly triaxial stress state in the DP and large W-NiWFe interface stresses. However, the NiWFe interface is strong, and WD local fracture modes are rare. The predominant local fracture modes are WC and WW, that produce small, particle-sized, microcracks. The small microcracks are arrested and subsequently blunted by the NiWFe DP honeycomb web (Figs. 1, 8b, 13, and 14). The web also bridges multiple coplanar microcracks that ultimately form. Thus the key ductile phase toughening (DPT) mechanism is shifted from the classical macrocrack bridging and deflection, to process zone microcrack arrest, blunting and bridging. Under these conditions, large scale bridging effects and arrest mechanisms stabilize the microcracks against propagation (see Fig. 8), in part due to the small dimensions of the W-particles and the corresponding initial microcracks (15 to 45 μ, averaging ≈ 27 ± 15 μm, see Table 6). Further, while the W particles remain encased in the DP, they can plastically deform under high stresses.

The most important consequence of this combination of micromechanisms is the large dissipation of plastic energy, partly due to the dilatational strains from the blunting microcracks, that also shield the crack tip fields, greatly reducing the local stress concentrations. Thus, the process zone deformation leading to crack growth resembles, in some ways, classical microvoid nucleation (initial microcracking), growth (microcrack blunting and opening) and coaleascence (microcrack linking and unstable growth), typical of highly ductile metals and alloys, such as low alloy RPV steels.

A simple dimensional ductile fracture cohesive zone plain strain model rationalizes the observed RT WHA toughness in terms of the tensile flow stress ($\sigma_{fl} \approx 750$ MPa), elastic modulus and Poisson's ratio ($E \approx 400$ GPa and $\nu \approx 0.28$) and the typical critical CTOD ($\delta_c \approx 35$ μm) observed at crack growth initiation as [56]:

$$K_{Jc} \approx \sqrt{[2\sigma_{fl}E\delta_c/(1-\nu_2)]} \approx 151 \text{ MPa}\sqrt{m}$$

Note K_{Jc} has a contribution from the process zone dilatation, as reflected in the large δ_c.

However, there are limits to toughening by microcrack bridging that emerge in tests below RT and at high W. The primary effect of lower temperature appears to be the increase in WC, leading to reductions in K_{Jm} or K_{Ic} with decreasing temperature, as illustrated in Figures 11 and 10d which plots the average local fracture mode percentages for all 4 W-NiFe WHAs as a function of temperature, along with the corresponding average K_{Jm}.

It appears that the decrease in fracture toughness and transition to elastic fracture is associated with the increased brittleness of W at lower temperature leading to more initial WC microcracks, which are not as isolated in fewer and more widely-spaced W particles. Below a transition temperature, that depends on the W loading, larger number of more proximate co-planar microcracks almost immediately link to form larger mesocracks that unstably propagate as an elastic fracture event. However, plastic rupture of the ligaments linking the microcracks still contributes to a higher WHA fracture toughness compared to monolithic W.

The tests at low temperature were aimed at assessing the effects of decreases in the W-particle K_{Ic}, associated with a corresponding increases in σ_y, as well as higher crack tip stress fields. While not fully representative, the low temperature tests may

partially emulate irradiation hardening that occurs at higher service temperatures. Figure 15 shows the K_{Jm} or K_{Ic} versus σ_y (T) for the 4 WHAs. K_{Jm} systematically decreases in toughness with increasing σ_y. Again, however, even at low temperature the WHAs K_{Ic} are still much larger than for monolithic W at RT. Assuming lower temperature is an approximate surrogate for neutron irradiation hardening, $\Delta\sigma_y$ up to 750 MPa may be tolerable in WHA plasma facing components. However, only the 90W WHA is able to avoid elastic fracture at $\Delta\sigma_y \approx 550$ MPa. At higher W, the corresponding hardening limit to avoid elastic fracture is $\Delta\sigma_y < \approx 200$ MPa.

There are many other open questions regarding the use of W-NiFe WHA for fusion divertor applications. First, and perhaps foremost, are size and geometry effects that are partially dealt with elsewhere [55] and are the subject of ongoing studies. Further, Ni is not a low activation element allowed in the class of normal reduced activation ferritic-martensitic steels. Thus the system level tolerance for limited amounts of Ni should be assessed. Further, these alloys will almost certainly be part of hybrid materials components, perhaps serving an intermediate crack arrest function like in a monolithic W:W-NiFe:ODS steel:Cu multilayer. The opportunities for using graded systems and additive manufacturing techniques for component fabrication are obvious. Other issues include temperature limits, phase stability, irradiation effects, DP and interface strength at higher temperature including in the creep regime, and integrated thermal-mechanical durability in the presence of high temperatures and time-varying very intense heat fluxes. However, further discussion of these issues is beyond the scope of this paper, which focuses on the new toughening mechanisms discovered in this work.

5. Conclusions

Comprehensive mechanical property characterization tests, including microhardness, tensile and fracture toughness, were conducted on a series of W-NiFe WHAs from 23°C down to -196°C. The key results and conclusions can be summarized as follows:

- Roughly spherical W particles are surrounded by a honeycomb web of a 50Ni30W20Fe (wt.%) solid solution DP following LPS. The reacted W particle size increases from ~17μm to ~ 38 μm and DP area percentage decreases from ~16% to ~6% between 90W and 97W with additional local inhomogeneity. The NiWFe DP thickness, $t \approx 4.9 \pm 4.6$ μm, is similar in all cases. The frequency of W-W bonded particles increases with increasing W.
- The average microhardness (H_v) at RT only slightly increases with increasing W fraction from 321 ± 9 kg/mm^2 for 90W to 344 ± 9 kg/mm^2 for 97W. The corresponding H_v almost doubles at -196°C, and increases from 507 ± 7 to 609 ± 21 kg/mm^2 between 90W and 97W.
- The RT σ_y also does not vary significantly with increasing W. However, σ_u as well as the uniform and total elongations ($\varepsilon_u \approx \varepsilon_t$) systematically decrease with higher W. The σ_y and σ_u increase and the ε_t decrease with decreasing temperature. Tensile elastic fracture ($\varepsilon_t = 0\%$) occurs at -100ºC for alloys with ≥ 95W and in all the W-NiFe WHAs at -196 ºC.
- The RT fracture toughness for the small specimens of 90 to 95W WHA alloys averages $K_{Jm} \approx 100 \pm 15$ MPa√m, decreasing to 69 ± 12 MPa√m at 97W. However, this K_{Jm} is still ≈ 9x higher than that of monolithic W, with a typical K_{Ic}

≈ 8 ± 4 MPa√m. Extensive stable crack growth occurs in all the specimen tests at RT.

- While there are multiple toughening mechanisms, the dominant effects of the DP is plasticizing the crack tip process zone including deformation of the normally brittle W particles, and dilatational energy dissipation and shielding, both due to stable arrested microcrack blunting.
- Low-temperature fracture toughness tests on small specimens were carried out down to -196 °C, to partly emulate irradiation hardening. K_{Jm} systematically decreases with decreasing temperature and increasing W. Transitions from stable crack growth to linear elastic fracture are approximately -150ºC, -100ºC, -75ºC and -25ºC for 90W, 92.5W, 95W and 97W, respectively. The K_{Jm} at this transition averages ≈ 50 ± 5 MPa√m which, again, is much higher that the elastic K_{Ic} ≈ 8 MPa√m
- There are a number of outstanding issues regarding the fracture toughness and use of W-NiFe WHA in divertor applications. While these topics are also beyond the scope of this paper, the database and insights developed here provide the foundation for future progress.

Acknowledgments

We gratefully acknowledge the support provided by U.S. Department of Energy through the Office of Fusion Energy Sciences (DOE 8-442520-22403-3 ROF02 and DOE Fusion 442520-224119). Our initial work on the W-FeNi WHA was inspired by our collaborations C. Henager and R. Kurtz at PNNL. We also thank our UCSB colleagues

K. Cunningham, S. Pal, K. Fields and D. Gragg for their important contributions to this work. The U.S. National Science Foundation supported California Nanoscience Institute provided facilities critical the success of this research.

References

[1] M. Rieth, S.L. Dudarev, S.M. Gonzalez De Vicente et al, Recent progress in research on tungsten materials for nuclear fusion applications in Europe, J. Nucl. Mater. 432 (2013) 482–500.

[2] P. Norajitra, R. Giniyatulin, W. Krauss, V. Kuznetsov, I. Mazul, I. Ovchinnikov, J. Reiser, M. Rieth, V. Widak, Current status of He-cooled divertor development for DEMO, Fusion Eng. Des. 84 (2009) 1429–1433.

[3] V. Philipps, Tungsten as material for plasma-facing components in fusion devices, J. Nucl. Mater. 415 (2011) S2–S9.

[4] J. Davis, V. Barabash, A. Makhankov, L. Plöchl, K. Slattery, Assessment of tungsten for use in the ITER plasma facing components, J. Nucl. Mater. 258–263 (1998) 308–312.

[5] C. Henager Jr, W. Setyawan, T. Roosendaal, N. Overman, B. Borlaug, E. Stevens, K. Wagner, R. Kurtz, G.R. Odette, B. Nguyen, K. Cunningham, Ductile-phase toughened tungsten for plasma-facing materials in fusion reactors, Int. J. Powder Metall. 53 (2017) 53–69.

[6] J. Reiser, J. Hoffmann, U. Jäntsch, M. Klimenkov, S. Bonk, C. Bonnekoh, M. Rieth, A. Hoffmann, T. Mrotzek, Ductilisation of tungsten (W): On the shift of the brittle-to-ductile transition (BDT) to lower temperatures through cold rolling, Int. J. Refract. Met. Hard Mater. 54 (2016) 351–369.

[7] B. Gludovatz, S. Wurster, A. Hoffmann, R. Pippan, Fracture toughness of polycrystalline tungsten alloys, Int. J. Refract. Met. Hard Mater. 28 (2010) 674–678.

[8] A.A.N. Németh, J. Reiser, D.E.J. Armstrong, M. Rieth, The nature of the brittle-to-ductile transition of ultra fine grained tungsten (W) foil, Int. J. Refract. Met. Hard Mater. 50 (2015) 9–15.

[9] L. Veleva, Contribution to the production and characterization of W-Y , W-Y2O3 and W-TiC materials for fusion reactors, PhD Thesis, Ec. Polytech. Fed. Lausanne, Switzarl. 4995 (2011).

[10] M. Battabyal, R. Schäublin, P. Spätig, M. Walter, M. Rieth, N. Baluc, Microstructure and mechanical properties of a W – 2wt .% Y2O3 composite produced by sintering and hot forging, J. Nucl. Mater. 442 (2013) S225–S228.

[11] J. Riesch, Y. Han, J. Almanstötter, J.W. Coenen, T. Höschen, B. Jasper, P. Zhao, C. Linsmeier, R. Neu, Development of tungsten fibre-reinforced tungsten composites towards their use in DEMO - Potassium doped tungsten wire, Phys. Scr. T167 (2016) 14006.

[12] A. Luo, D.L. Jacobson, K.S. Shin, Solution softening mechanism of iridium and rhenium in tungsten at room temperature, Refract. Met. Hard Mater. 10 (1991)

107–114.
[13] P.L. Raffo, Yielding and fracture in tungsten and tungsten-rhenium alloys, J. Less-Common Met. 17 (1969) 133–149.
[14] L. Romaner, C. Ambrosch-Draxl, R. Pippan, Effect of rhenium on the dislocation core structure in tungsten, Phys. Rev. Lett. 104 (2010) 1–4.
[15] W.D. Klopp, Review of ductilizing of Group VIA elements by rhenium and other solutes, in: NASA Tech. Note, D-4955, Lewis Res. Cent. Cleveland, Ohio, 1968: pp. 1–37.
[16] W.D. Klopp, A review of chromium, molybdenum, and tungsten alloys, J. Less-Common Met. 42 (1975) 261–278.
[17] E. Tejado, P.A. Carvalho, A. Munoz, M. Dias, J.B. Correia, U. V. Mardolcar, J.Y. Pastor, The effects of tantalum addition on the microtexture and mechanical behaviour of tungsten for ITER applications, J. Nucl. Mater. 467 (2015) 949–955.
[18] P. Krautwasser, H. Derz, E. Kny, Influence of fast neutron fluence on the DBTT of tungsten, W10Re and W3.4Ni1.6Fe, Report no: OEFZS-A-3304, vol 30, Austria, 1995.
[19] J. Reiser, S. Wurster, J. Hoffmann, S. Bonk, C. Bonnekoh, D. Kiener, R. Pippan, A. Hoffmann, M. Rieth, Ductilisation of tungsten (W) through cold-rolling: R-curve behaviour, Int. J. Refract. Met. Hard Mater. 58 (2016) 22–33.
[20] K.T. Venkateswara Rao, G.R. Odette, R.O. Ritchie, Ductile-reinforcement toughening in γ-TiAl intermetallic-matrix composites: Effects on fracture toughness and fatigue-crack propagation resistance, Acta Metall. Mater. 42 (1994) 893–911.
[21] G.R. Odette, B.L. Chao, J.W. Sheckherd, G.E. Lucas, Ductile phase toughening mechanisms in a TiAl-TiNb laminate composite, Acta Metall. Mater. 40 (1992) 2381–2389.
[22] M.G. Mendiratta, J.J. Lewandowski, D.M. Dimiduk, Strength and ductile-phase toughening in the two-phase Nb/Nb5Si3 alloys, Metall. Trans. A. 22 (1991) 1573–1583.
[23] L.S. Sigl, P.A. Mataga, B.J. Dalgleish, R.M. McMeeking, A.G. Evans, On the toughness of brittle materials reinforced with a ductile phase, Acta Metall. 36 (1988) 945–953.
[24] D. V. Edmonds, P.N. Jones, Interfacial embrittlement in liquid-phase sintered tungsten heavy alloys, Metall. Trans. A. 10 (1979) 289–295.
[25] B.C. Muddle, Interphase boundary precipitation in liquid phase sintered W-Ni-Fe and W-Ni-Cu alloys, Metall. Trans. A. 15 (1984) 1089–1098.
[26] A. Mondal, D. Agrawal, A. Upadhyaya, Microwave sintering of refractory metals / alloys : Microwave Sintering of Refractory Metals / alloys : W , Mo , Re , W-Cu , W-Ni-Cu and W-Ni-Fe Alloys, J. Microw. Power Electromagn. Energy. 44 (2010) 28–44.
[27] Z.A. Hamid, S.F. Moustafa, W.M. Daoush, F.A. Mouez, M. Hassan, Fabrication and characterization of tungsten heavy alloys using chemical reduction and mechanical alloying methods, Open J. Appl. Sci. 03 (2013) 15–27.
[28] M. Scapin, Mechanical characterization and modeling of the heavy tungsten alloy IT180, Int. J. Refract. Met. Hard Mater. 50 (2015) 258–268.
[29] X. Gong, J. Fan, F. Ding, Tensile mechanical properties and fracture behavior of

tungsten heavy alloys at 25-1100 °C, Mater. Sci. Eng. A. 646 (2015) 315–321.
[30] K. Hu, X. Li, X. Ai, S. Qu, Y. Li, Fabrication, characterization, and mechanical properties of 93W-4.9Ni-2.1Fe/95W-2.8Ni-1.2Fe/95W-2.8Ni-1.2Fe-1Al2O3 heavy alloy composites, Mater. Sci. Eng. A. 636 (2015) 452–458.
[31] U.R. Kiran, A. Panchal, M. Sankaranarayana, G.V.S.N. Rao, T.K. Nandy, Effect of alloying addition and microstructural parameters on mechanical properties of 93% tungsten heavy alloys, Mater. Sci. Eng. A. 640 (2015) 82–90.
[32] M.B. Shongwe, S. Diouf, M.O. Durowoju, P.A. Olubambi, M.M. Ramakokovhu, B.A. Obadele, A comparative study of spark plasma sintering and hybrid spark plasma sintering of 93W-4.9Ni-2.1Fe heavy alloy, Int. J. Refract. Met. Hard Mater. 55 (2016) 16–23.
[33] R. German, J. Hanafee, S. DiGiallonardo, Toughness variation with test temperature and cooling rate for liquid phase sintered W-3.5Ni-1.5Fe, Metall. Trans. A. 15 (1984) 121–128.
[34] K.S. Churn, R.M. German, Fracture behavior of W-Ni-Fe heavy alloys, Metall. Trans. A, Phys. Metall. Mater. Sci. 15 A (1984) 331–338.
[35] D. V Edmonds, Structure/property relationships in sintering heavy alloys, Refract. Met. Hard Mater. 10 (1991) 15–26.
[36] R.M. German, A. Bose, S.S. Mani, Sintering time and atmosphere influences on the microstructure and mechanical properties of tungsten heavy alloys, Metall. Trans. A. 23 (1992) 211–219.
[37] K.M.O. Zamora, J.G. Sevillano, M.F. Perez, Fracture toughness of W heavy metal alloys, Mater. Sci. Eng. A. 157 (1992) 151–160.
[38] A. Upadhyaya, Processing strategy for consolidating tungsten heavy alloys for ordnance applications, Mater. Chem. Phys. 67 (2001) 101–110.
[39] Z.H. Zhang, F.C. Wang, S.K. Li, L. Wang, Deformation characteristics of the 93W-4.9Ni-2.1Fe tungsten heavy alloy deformed by hydrostatic extrusion, Mater. Sci. Eng. A. 435–436 (2006) 632–637.
[40] S. Islam, X. Qu, X. He, Investigation of composition and microstructure effect on fracture behaviour of tungsten heavy alloys, Powder Metall. 50 (2007) 11–13.
[41] Y. Şahin, Recent progress in processing of tungsten heavy alloys, J. Powder Technol. 2014 (2014) 1–22.
[42] R. Neu, H. Maier, M. Balden, S. Elgeti, H. Gietl, H. Greuner, A. Herrmann, A. Houben, V. Rohde, B. Sieglin, I. Zammuto, Investigations on tungsten heavy alloys for use as plasma facing material, Fusion Eng. Des. 124 (2017) 450–454.
[43] R. Neu, H. Maier, M. Balden, R. Dux, S. Elgeti, H. Gietl, H. Greuner, A. Herrmann, T. Höschen, M. Li, V. Rohde, D. Ruprecht, B. Sieglin, I. Zammuto, Results on the use of tungsten heavy alloys in the divertor of ASDEX Upgrade, J. Nucl. Mater. 511 (2018) 567–573.
[44] G. V Raynor, V.G. Rivlin, Phase equilibria in iron ternary alloys: Critical evaluation of constitutions of certain ternary alloys containing iron , tungsten , and a third metal, Int. Met. Rev. 26 (1981) 213–249.
[45] J.H. You, Design feasibility study of a divertor component reinforced with fibrous metal matrix composite laminate, J. Nucl. Mater. 336 (2005) 97–109.
[46] ASTM E1921-03, Standard Test Method for Determination of Reference Temperature , To , for Ferritic Steels in the Transition Range, in: Annu. B. ASTM

Stand., ASTM International, 100 Barr Harbor Drive, PO Box C700, West Conshohocken, PA 19428-2959, United States, 2012: pp. 1–25.
[47] A.G. Evans, R.M. Cannon, Toughening of b rittle solids by martensitic transformations, Acta Metall. 34 (1986) 761–800.
[48] J.W. Hutchinson, Non-linear fracture mechanics, Tech. Univ. of Denmark, 1979.
[49] M. Rühle, A.G. Evans, R.M. McMeeking, P.G. Charalambides, J.W. Hutchinson, Microcrack toughening in alumina/zirconia, Acta Metall. 35 (1987) 2701–2710.
[50] A.G. Evans, Z.B. Ahmad, D.G. Gilbert, P.W.R. Beaumont, Mechanisms of toughening in rubber toughened polymers, Acta Metall. 34 (1986) 79–87.
[51] M.E. Alam, S. Pal, K. Fields, S.A. Maloy, D.T. Hoelzer, G.R. Odette, Tensile deformation and fracture properties of a 14YWT nanostructured ferritic alloy, Mater. Sci. Eng. A. 675 (2016) 437–448.
[52] ASTM E8M-15a, ASTM E8/E8M - 15a: Standard test methods for tension testing of metallic materials, in: Annu. B. ASTM Stand., ASTM International, 100 Barr Harbor Drive, PO Box C700, West Conshohocken, PA 19428-2959, United States, 2015.
[53] M.E. Alam, S. Pal, S.A. Maloy, G.R. Odette, On delamination toughening of a 14YWT nanostructured ferritic alloy, Acta Mater. 136 (2017) 61–73.
[54] ASTM C1421-16, Standard Test Methods for Determination of Fracture Toughness of Advanced Ceramics at Ambient Temperature, in: Annu. B. ASTM Stand., ASTM International, 100 Barr Harbor Drive, PO Box C700, West Conshohocken, PA 19428-2959. United States, 2016: pp. 1–33.
[55] M.E. Alam, G.R. Odette, On the effect of specimen size, geometry and ductile phase content on the fracture toughness of tungsten heavy metal alloys, DOE Fusion React. Mater. Progr. Semiannu. Prog. Rep. DOE0313/66 (2019) 45–52.
[56] T.L. Anderson, Fracture Mechanics: Fundamentals and Applications, 3rd ed., Taylor & Francis Group, FL, USA, 2005.
[57] M.E. Alam, S. Pal, K. Fields, G.R. Odette, Mechanical properties characterization of 90-97wt% WNiFe heavy alloys, DOE Fusion React. Mater. Progr. Semiannu. Prog. Rep. DOE0313/61 (2016) 73–82.

List of Figures

Fig. 9 The low temperatures S specimen precracked 3PB P-d curves, normalized to a/W=0.5 for: (a) 90W; (b) 92.5W; (c) 95W; and, (d) 97W.

Fig. 10 Maximum load K_{Jm}: (a) 90W; (b) 95W; (c) 97W alloys as a function of temperature; and, (d) the average local fracture mode percentages as a function of temperature, along with the corresponding average K_{Jm} or K_{Ic} for all the 4 WHAs for tests using small specimens.

Fig. 11 SEM fractographs for the: (a) 90W, and (b) 97W bend bars along with corresponding WC fraction (%) as a function of test temperature.

Fig. 12 SEM RT tensile specimen side views showing: (a) stable WC, WW, WD microcracking and microcrack arrest and blunting, as well as W-particle deformation near the fracture surface of the 90W alloy; (b) numerous WC and WW microcracks for 97W WHA that are less blunted; and, (c and d) largely undeformed, crack-free W-particles for 90W and 97W, respectively, tested at -196ºC that failed by elastic fracture. The bottom row of images shows side-surface images of the deformation and local fracture mechanisms.

Fig. 13 SEM side surface views for the: (a) 90, and (b) 97W at RT; and, (c) 90W, and (d) 97W at -196ºC. RT test shows numerous micro-cleavage cracks and pores, while the -196ºC test shows propagation of the macrocrack before a population of microcracks form (note, the dark region around the propagating cracks are alcohol stains).

Fig. 14 (a and b) Side surface views of an identical location in a 95W alloy before and after deformation, respectively, showing a large number of arrested microcracks and dilatation (small boxes); (c) a 3D depth scan showing the lateral contraction in a 90W alloy near the crack tip; and (d) schematic illustrating the toughening mechanisms.

Fig. 15 Toughness (K_{Jm} or K_{Ic}) versus the estimated W yield strength (σ_y) for the various WNiFe WHAs. The filled and unfilled symbols represent stable crack growth and elastic (unstable) fracture, respectively, while the half-filled symbols represent mixed stable and unstable crack growth. The K_{Ic} for monolithic (unalloyed) W is also shown.

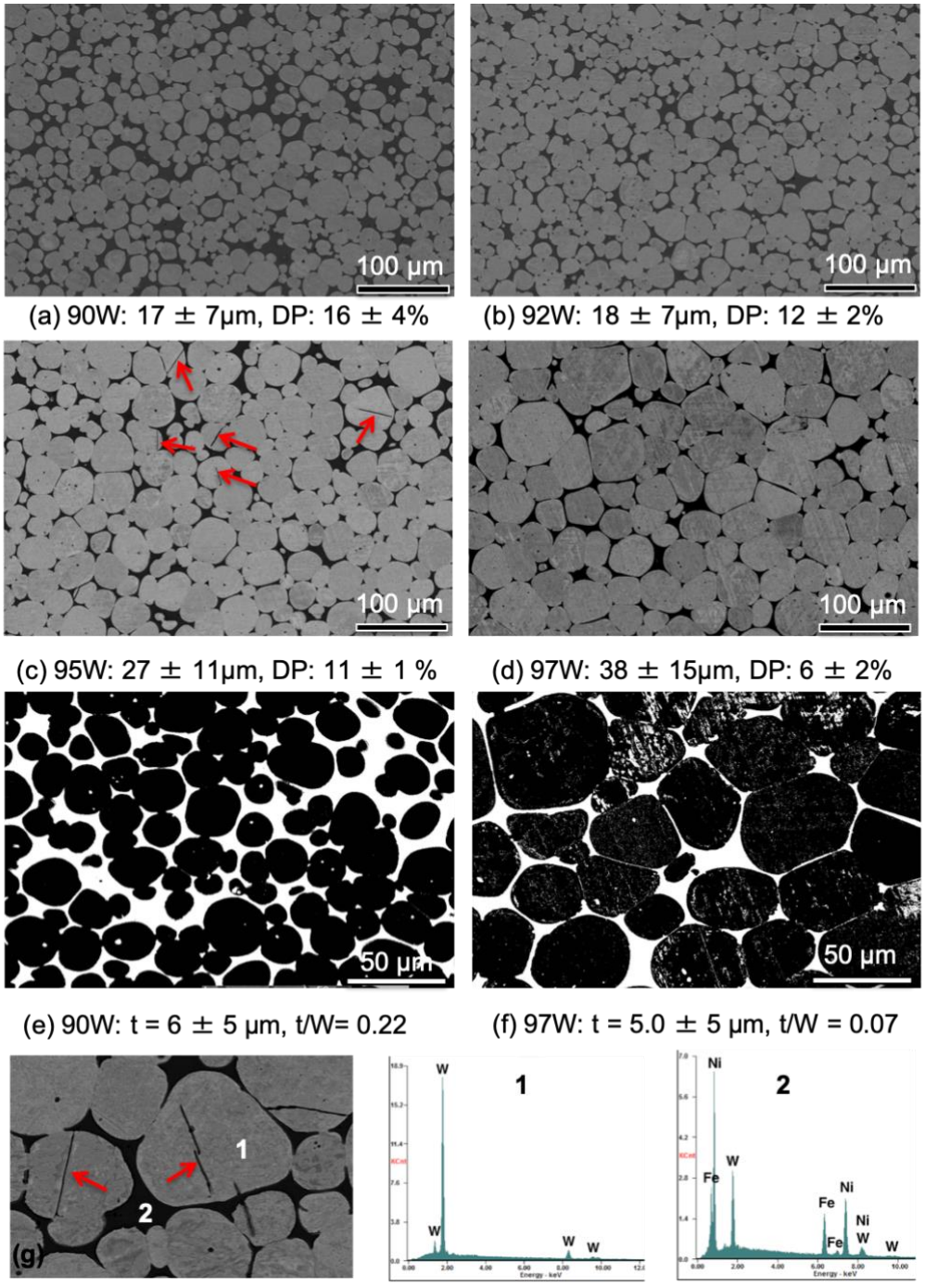

Fig. 1 SEM images of the W particles (gray) and the ductile NiWFe phase (black) for: (a) 90W, (b) 92.5W, (c) 95W, and (d) 97W WHA, respectively. The binary black (W) and white (NiWFe) images of: (e) 90W, and (f) 97W highlight the NiWFe honeycomb web characterized by the web thickness (t), and the t/W, thickness to W particle fraction ratio. Fig. (g) shows cracked W particles (short red arrows) in the as-received condition. Point 1 and 2 in (g) show EDS spectra for the unalloyed W phase and NiWFe ductile phase, respectively.

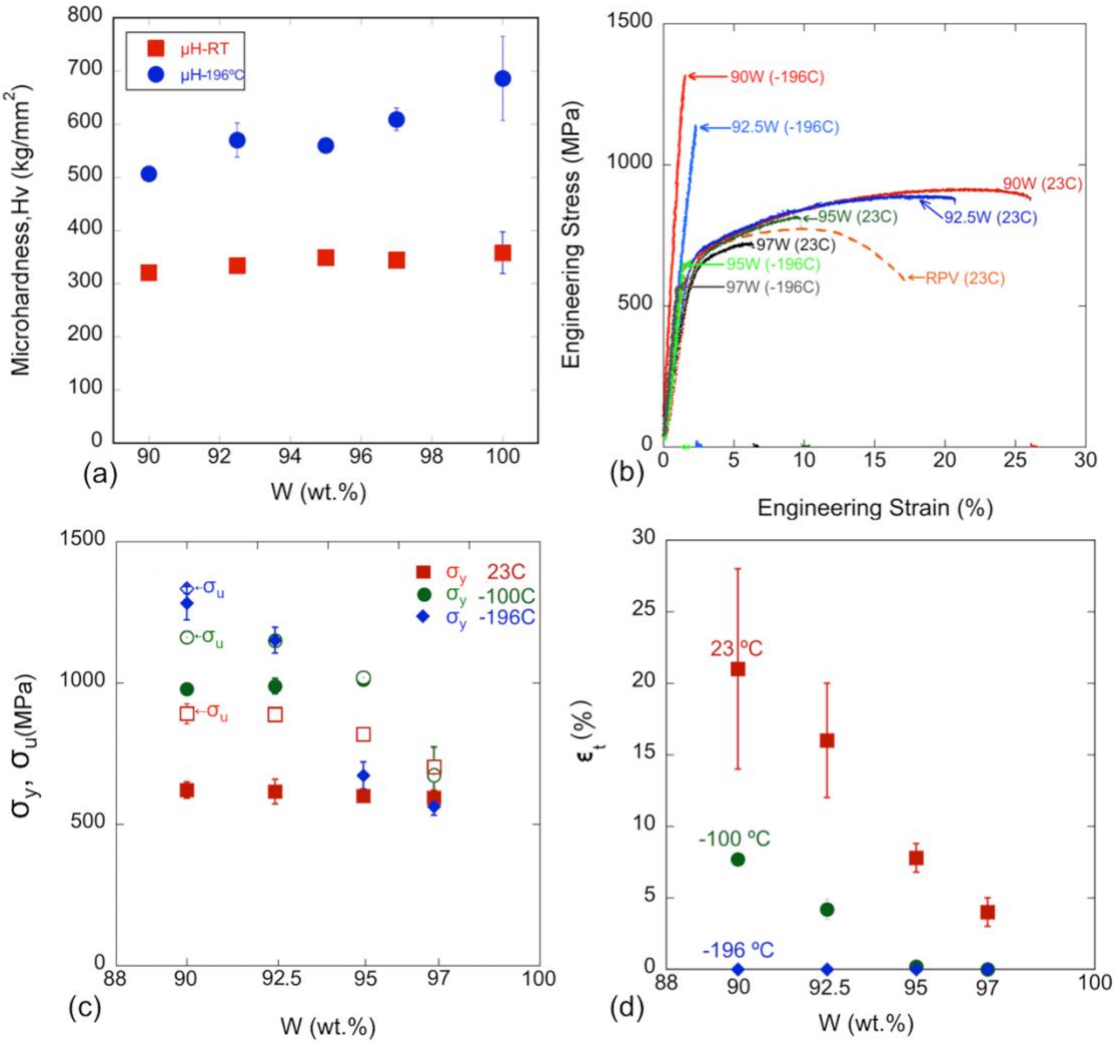

Fig. 2 WHA tensile properties and hardness as a function of W content and temperature: (a) Vickers microhardness (H_v); (b) engineering stress-strain (σ-ε) curves; (c) the 0.2% yield (σ_y: filled symbols) and ultimate tensile (σ_u: unfilled symbols) stresses; and, (d) the total elongations (ε_t).

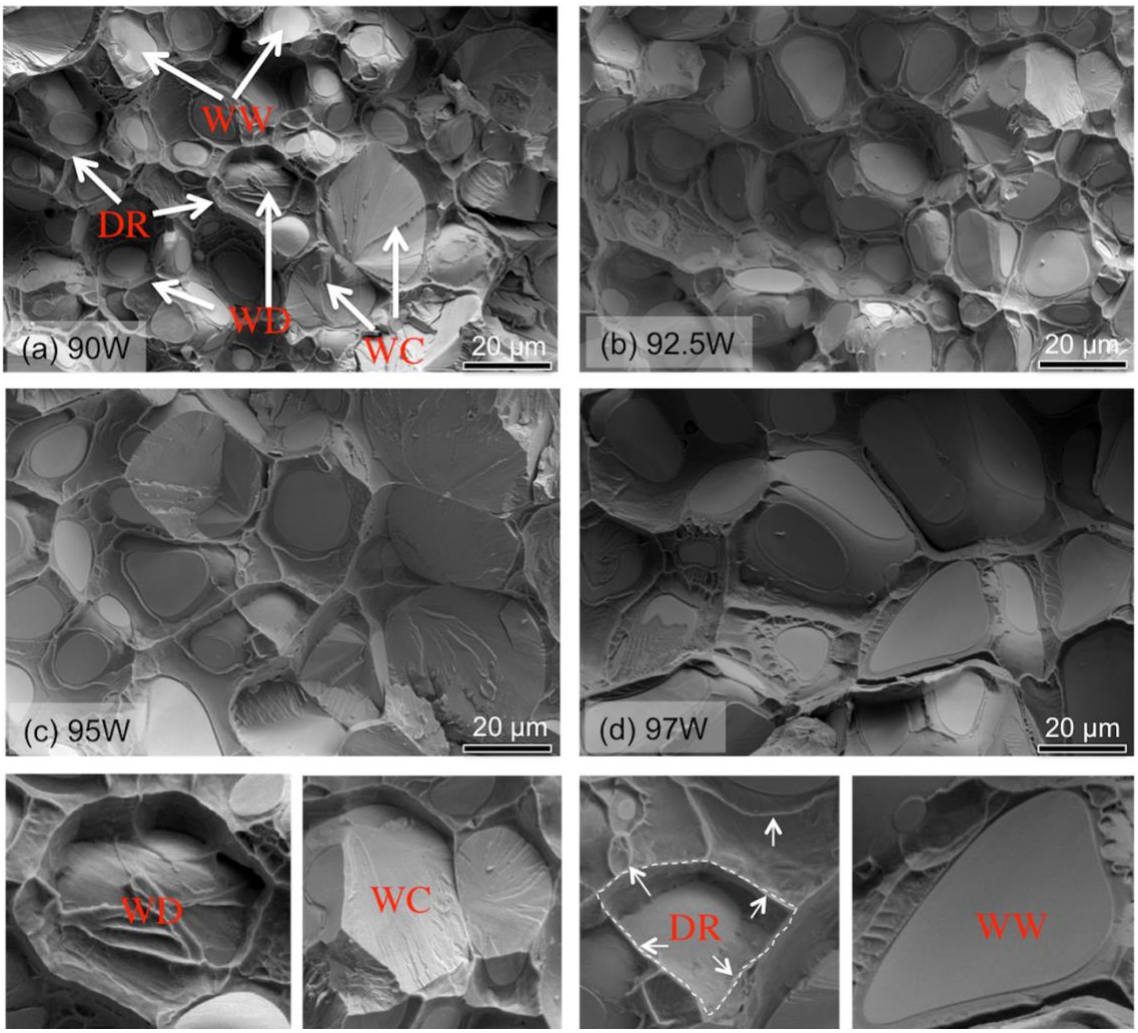

Fig. 3 SEM RT tensile test fractographs for: (a) 90W, (b) 92.5W, (c) 95W, and (d) 97W showing the four basic fracture modes: WD - W particle-NiWFe ductile phase interface decohesion; WC - W particle cleavage; DR - NiWFe ductile phase rupture; and, WW – W-W inter particle fracture. Magnified views of these various processes are shown in the bottom row of figures.

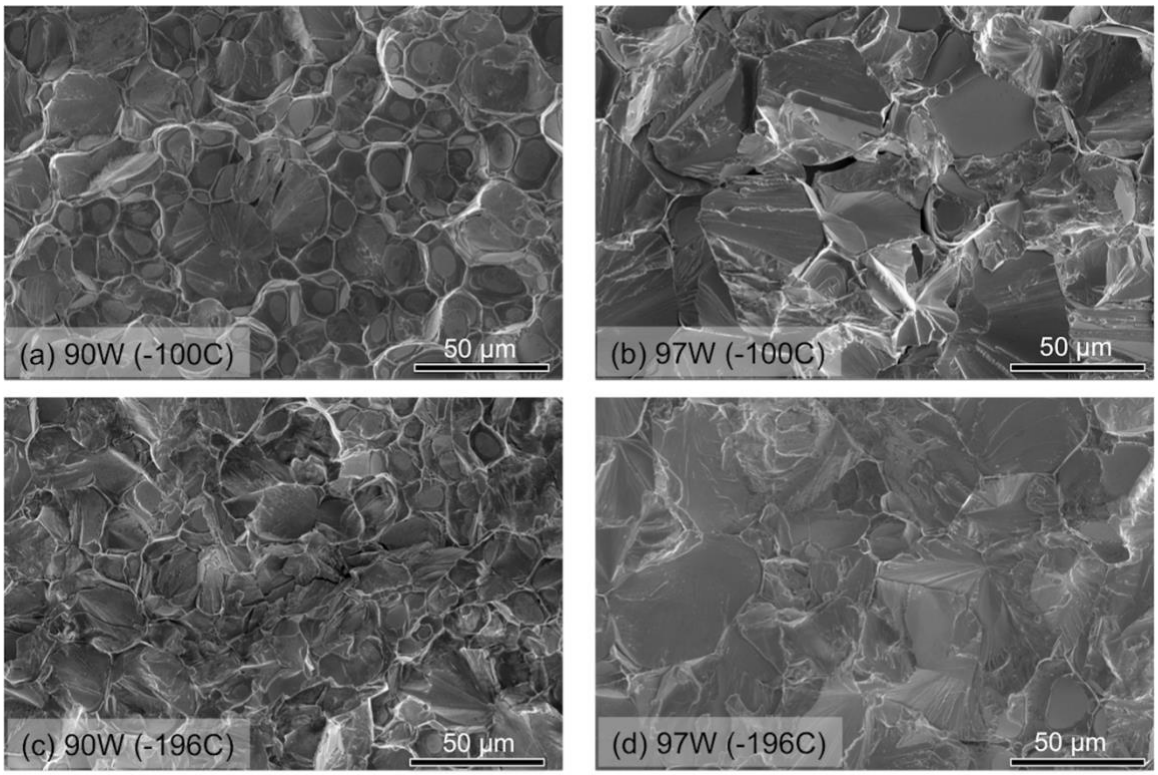

Fig. 4 SEM fractographs showing the fracture surfaces for the 90W (left) and 97W (right) for tensile tests at -100ºC (a-b) and -196ºC (c-d).

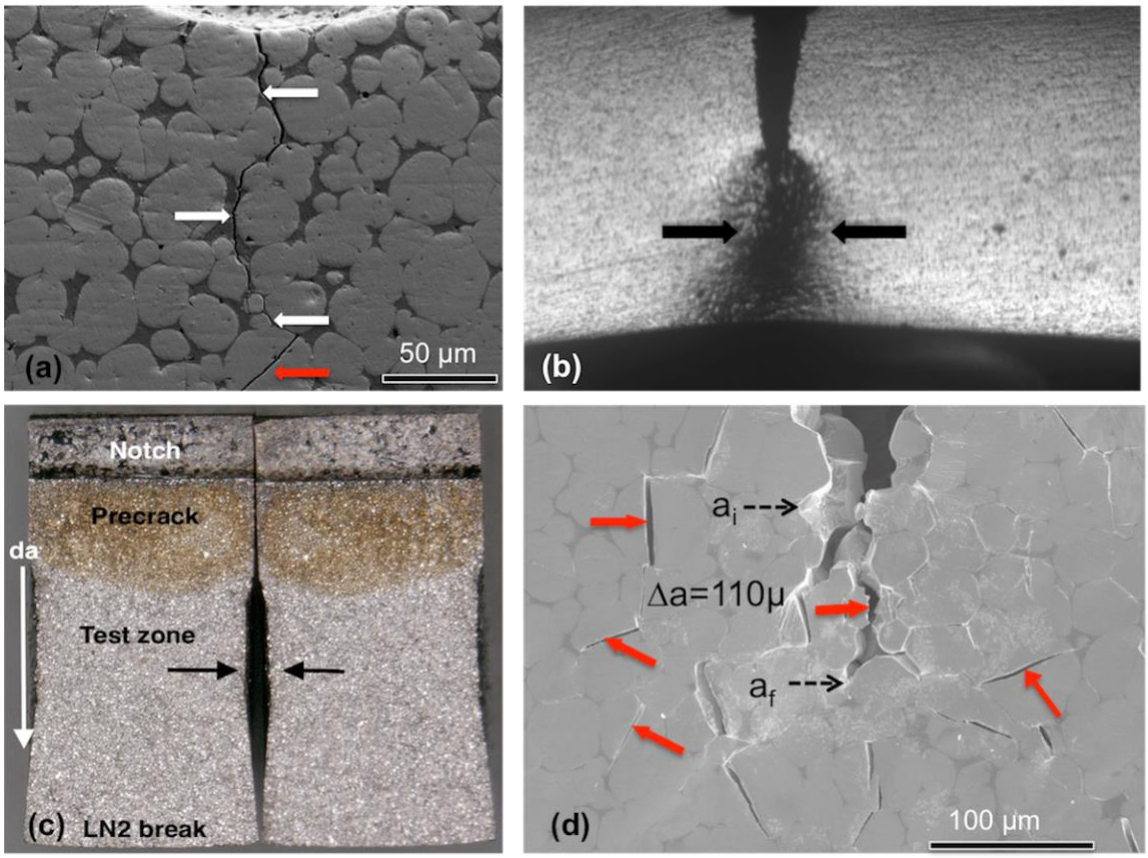

Fig. 5 (a) A SEM image showing the fatigue cracks mainly propagate through the matrix phase (white arrows); (b, c) optical images showing lateral contraction at the plastic zone (black arrows); and, (d) transgranular (red arrows) cracks, a small amount of crack extension ($\Delta a < 200\mu m$) during loading, accompanied by extensive arrested microcracking.

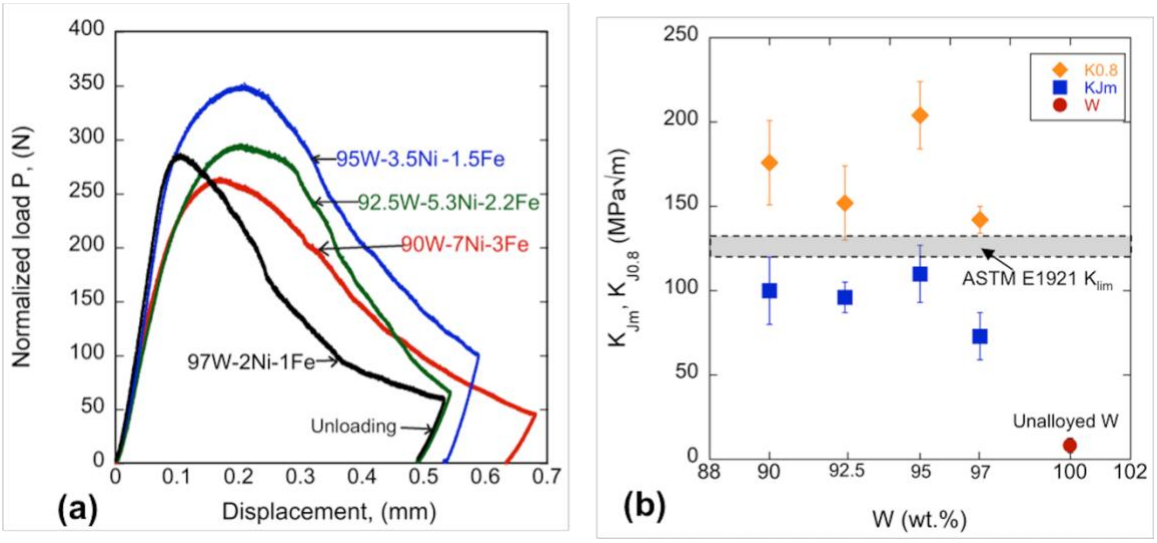

Fig. 6 (a) RT P-d curves normalized to a/W=0.5 showing extensive stable crack growth; and, (b) the average K_{Jm} and $K_{J0.8m}$ of W-NiFe WHAs at P_m and $P/P_m \approx 0.8$. The ASTM E1921 K_{lim} ($\approx$ 120-132 MPa$\sqrt{m}$) is also shown (gray rectangle). The actual crack extension is less than 200μm down to $P/P_m \approx 0.8$.

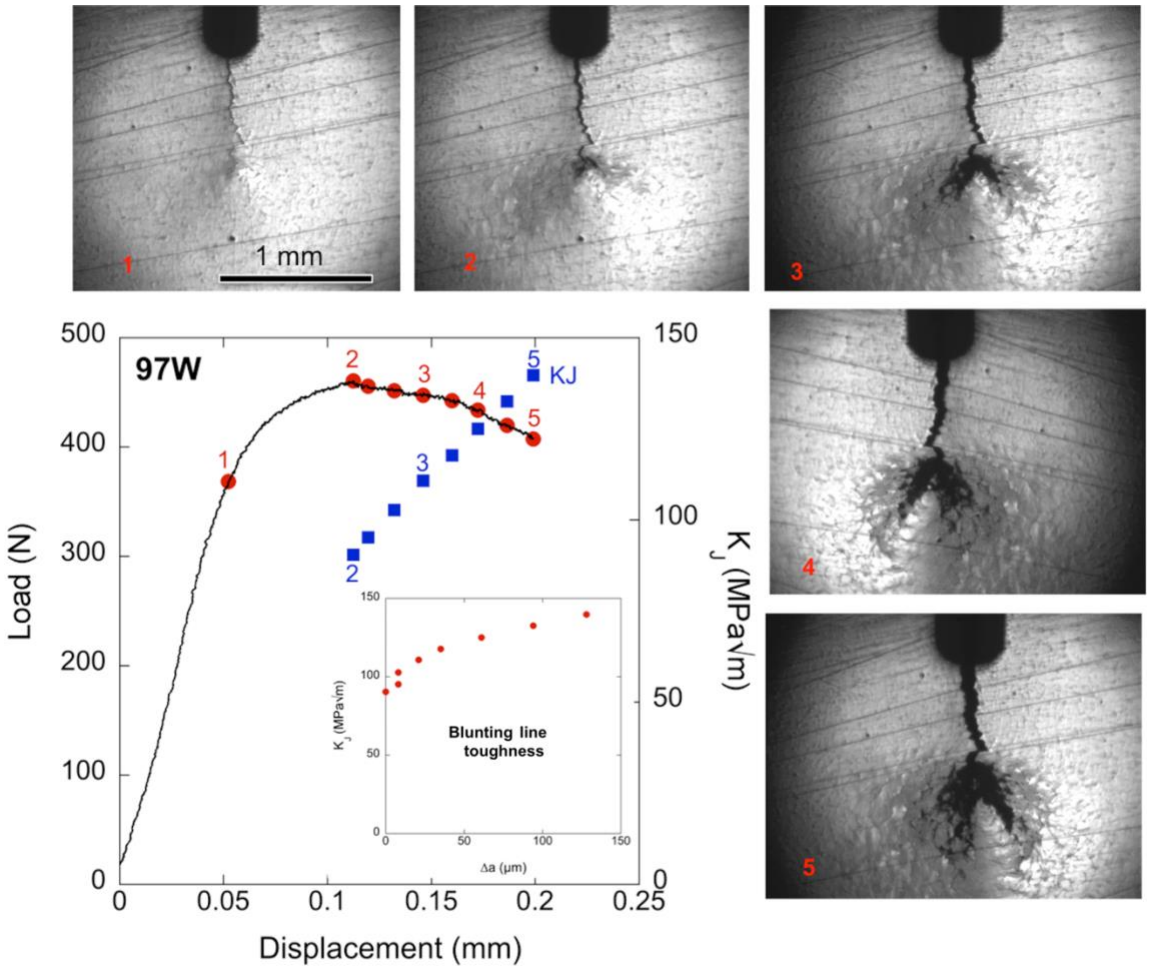

Fig. 7 RT 97W WHA P-d curve with *in-situ* optical images showing the formation of a plastic zone indicated by the dark area, in front of the crack tip, that is out of focus due to lateral contraction. The red circles are P-d points and blue squares are their corresponding K_J values.The insert shows J-Δa based on optical and SEM image analysis. Note that the total crack extension is ≈ 130μ, corresponding to a blunting line toughness of ≈ 139 MPa√m.

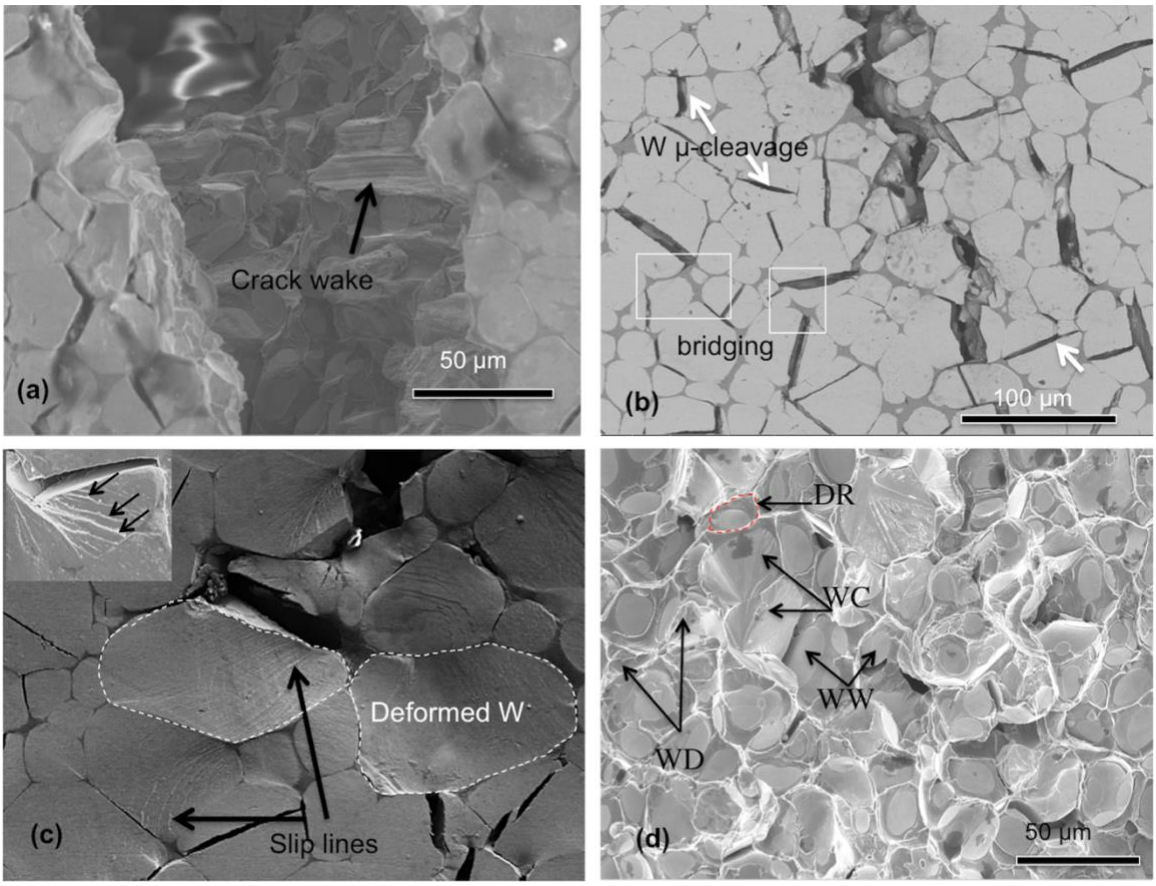

Fig. 8 SEM images illustrating: (a) crack wake bridging; (b) stable microcracks and bridging; (c) slip lines in the deformed W-particles; and, (d) various local fracture modes.

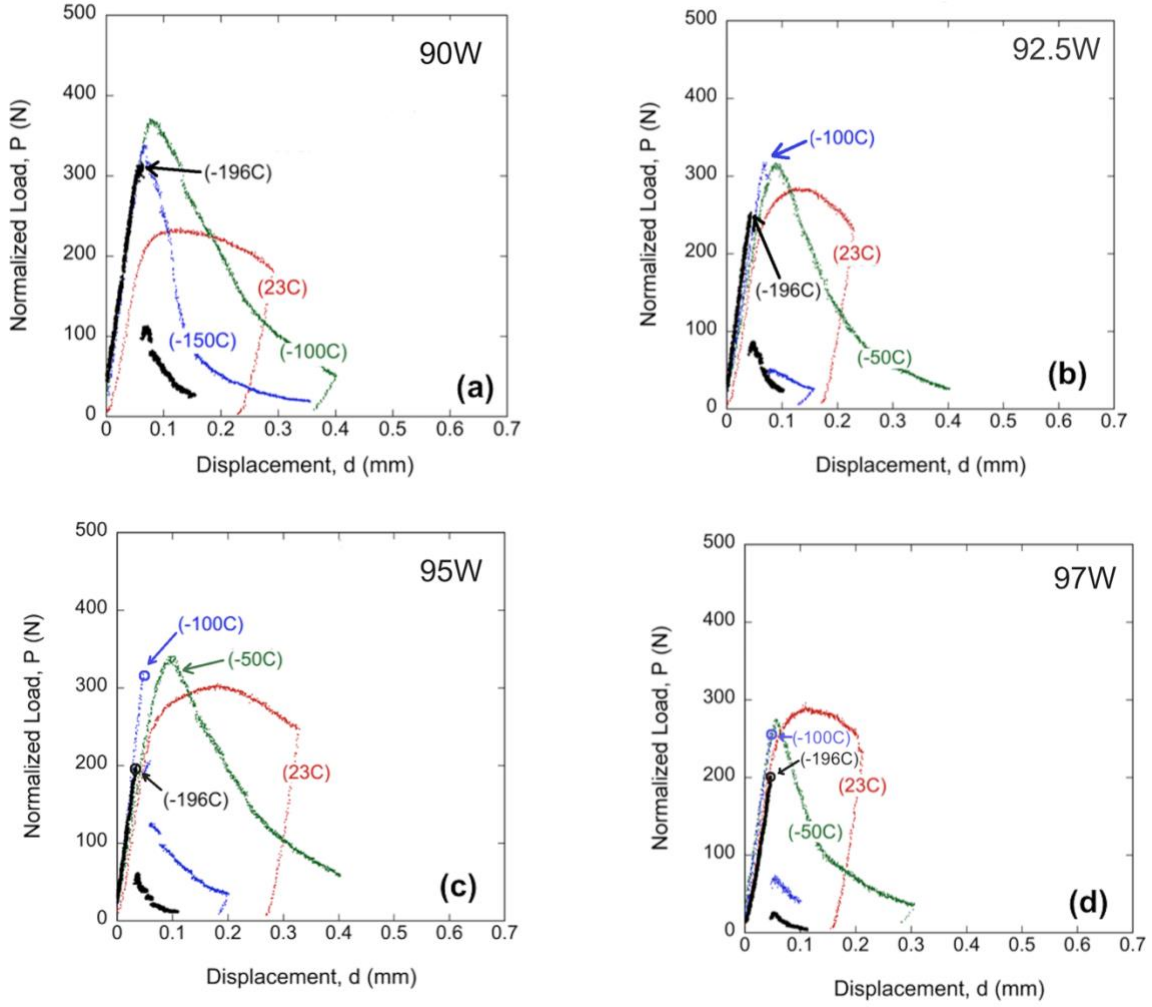

Fig. 9 The low temperatures S specimen precracked 3PB P-d curves, normalized to a/W=0.5 for: (a) 90W; (b) 92.5W; (c) 95W; and, (d) 97W.

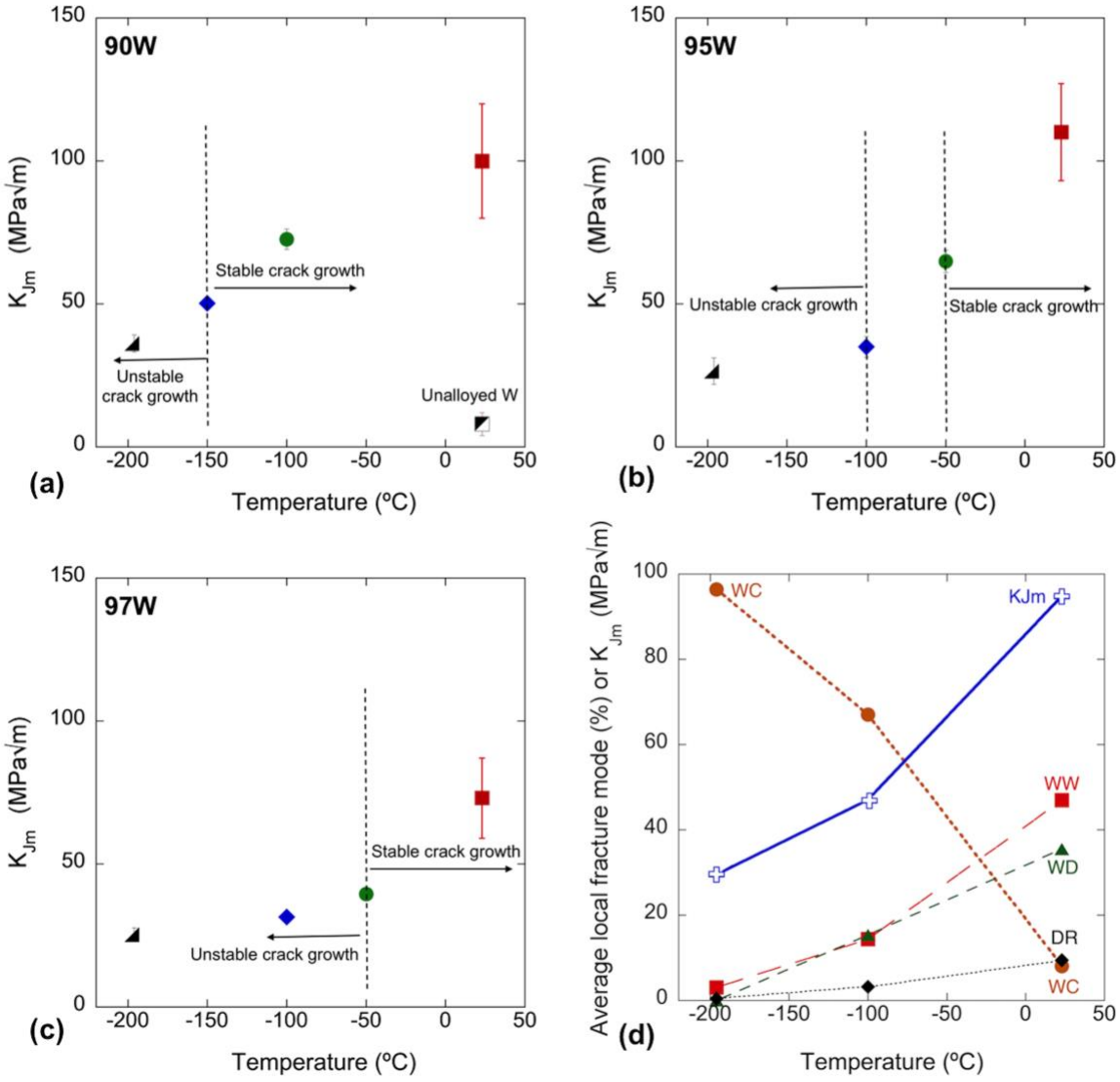

Fig. 10 Maximum load K_{Jm}: (a) 90W; (b) 95W; (c) 97W alloys as a function of temperature; and, (d) the average local fracture mode percentages as a function of temperature, along with the corresponding average K_{Jm} or K_{Ic} for all the 4 WHAs for tests using small specimens.

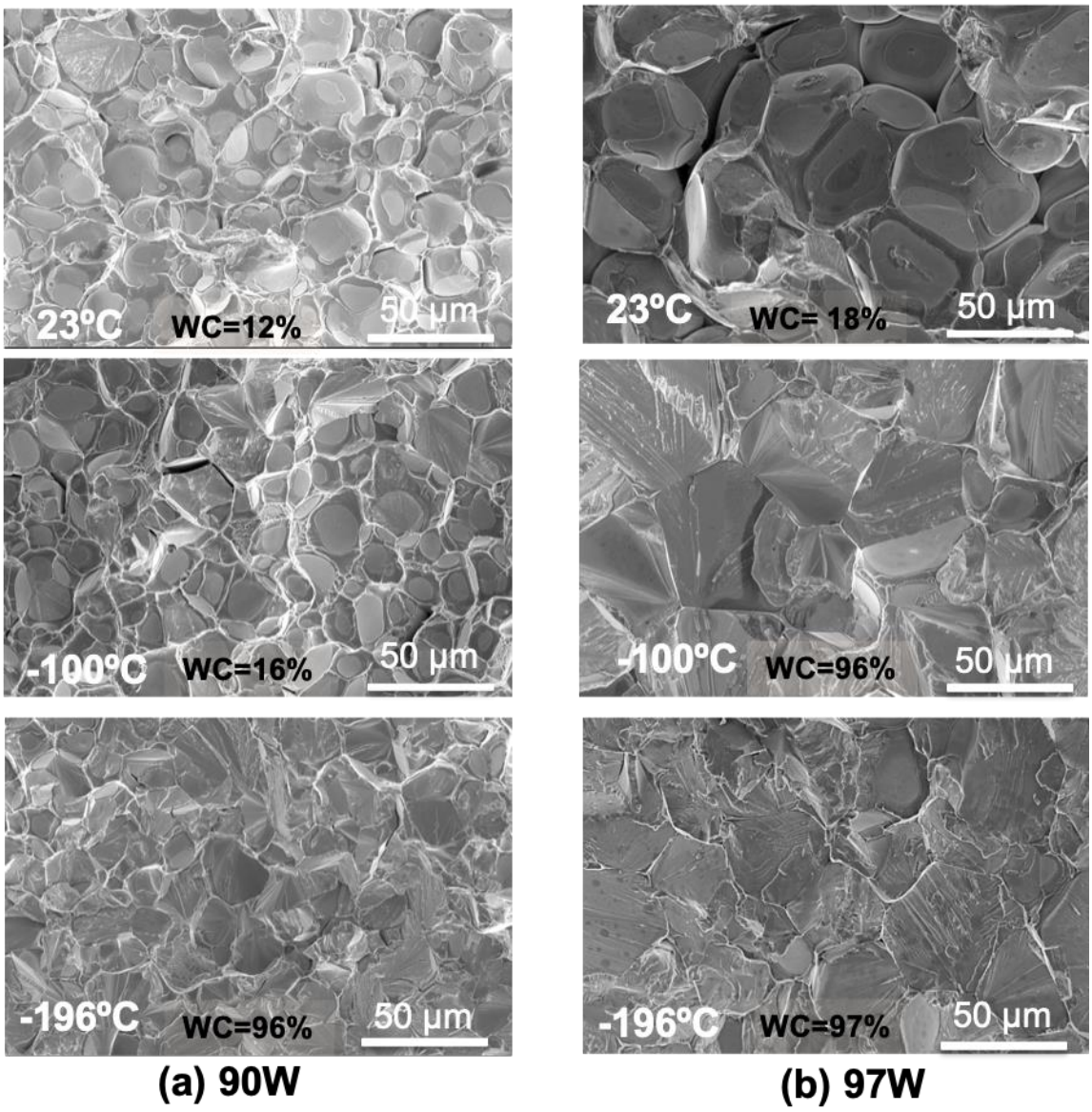

Fig. 11 SEM fractographs for the: (a) 90W, and (b) 97W bend bars along with corresponding WC fraction (%) as a function of test temperature.

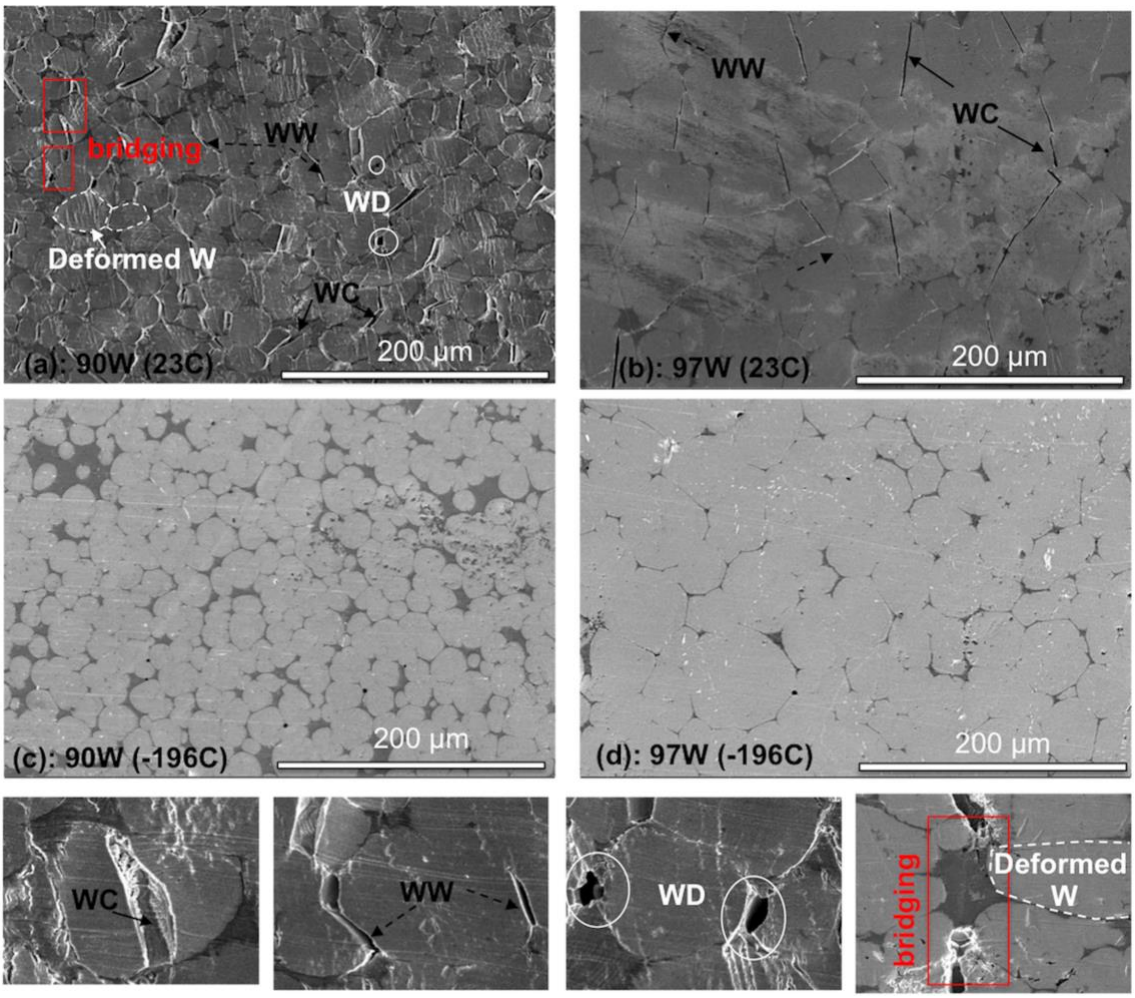

Fig. 12 SEM RT tensile specimen side views showing: (a) stable WC, WW, WD microcracking and microcrack arrest and blunting, as well as W-particle deformation near the fracture surface of the 90W alloy; (b) numerous WC and WW microcracks for 97W WHA that are less blunted; and, (c and d) largely undeformed, crack-free W-particles for 90W and 97W, respectively, tested at -196ºC that failed by elastic fracture. The bottom row of images shows side-surface images of the deformation and local fracture mechanisms.

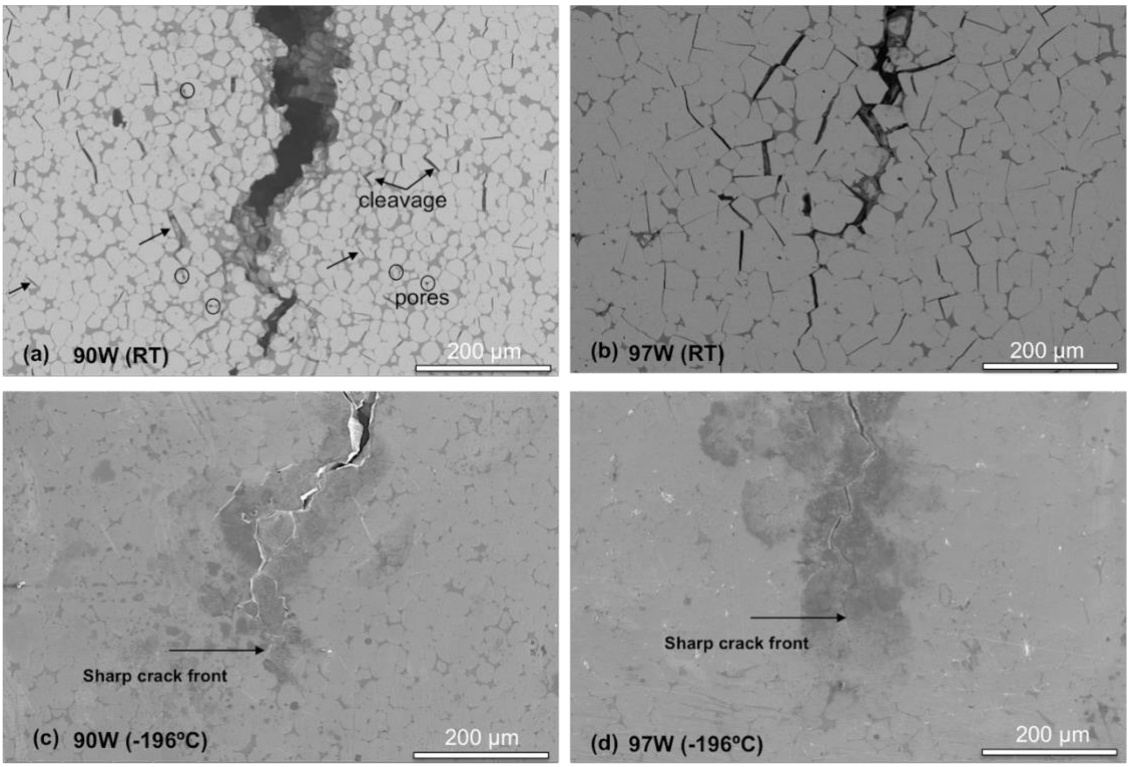

Fig. 13 SEM side surface views for the: (a) 90, and (b) 97W at RT; and, (c) 90W, and (d) 97W at -196ºC. RT test shows numerous micro-cleavage cracks and pores, while the -196ºC test shows propagation of the macrocrack before a population of microcracks form (note, the dark region around the propagating cracks are alcohol stains).

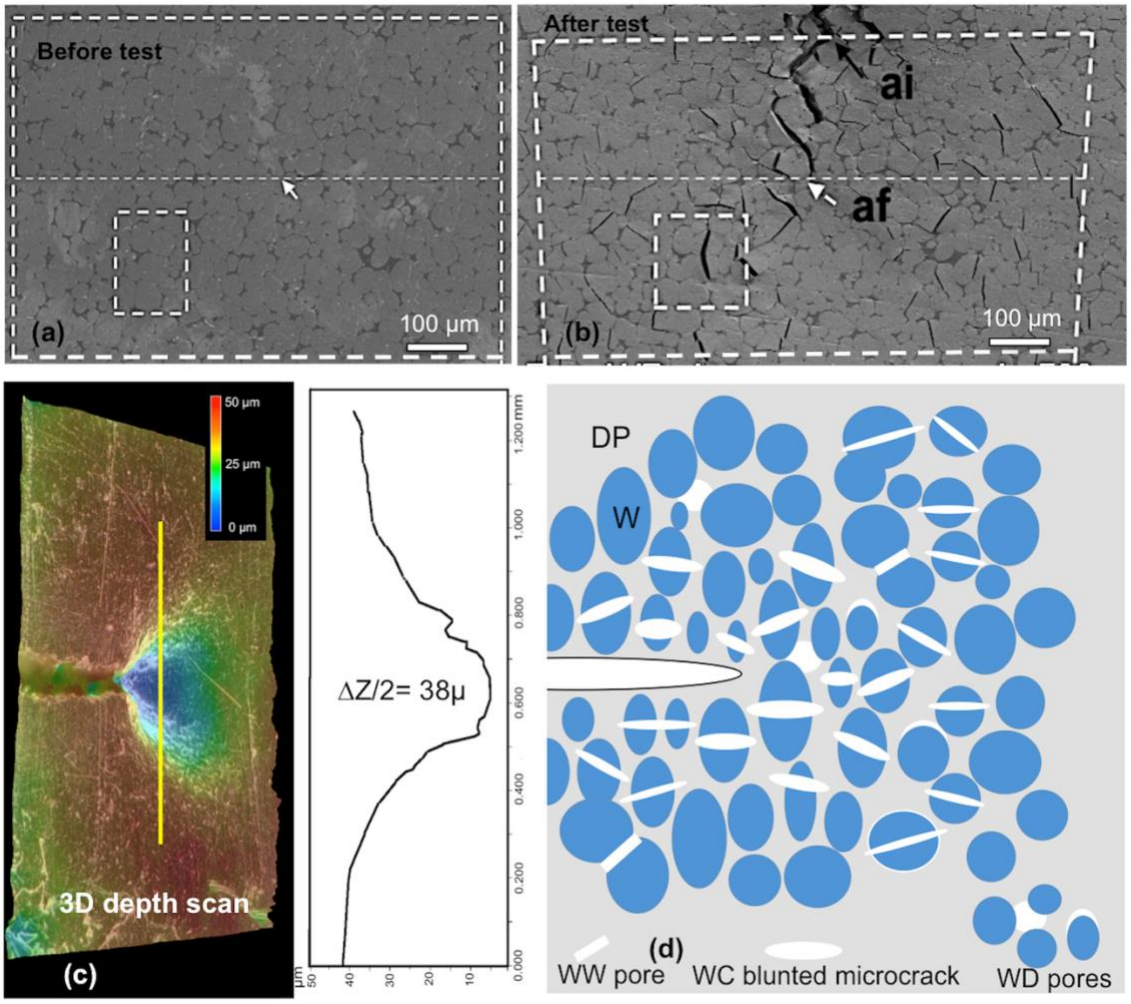

Fig. 14 (a and b) Side surface views of an identical location in a 95W alloy before and after deformation, respectively, showing a large number of arrested microcracks and dilatation (small boxes); (c) a 3D depth scan showing the lateral contraction in a 90W alloy near the crack tip; and (d) schematic illustrating the toughening mechanisms.

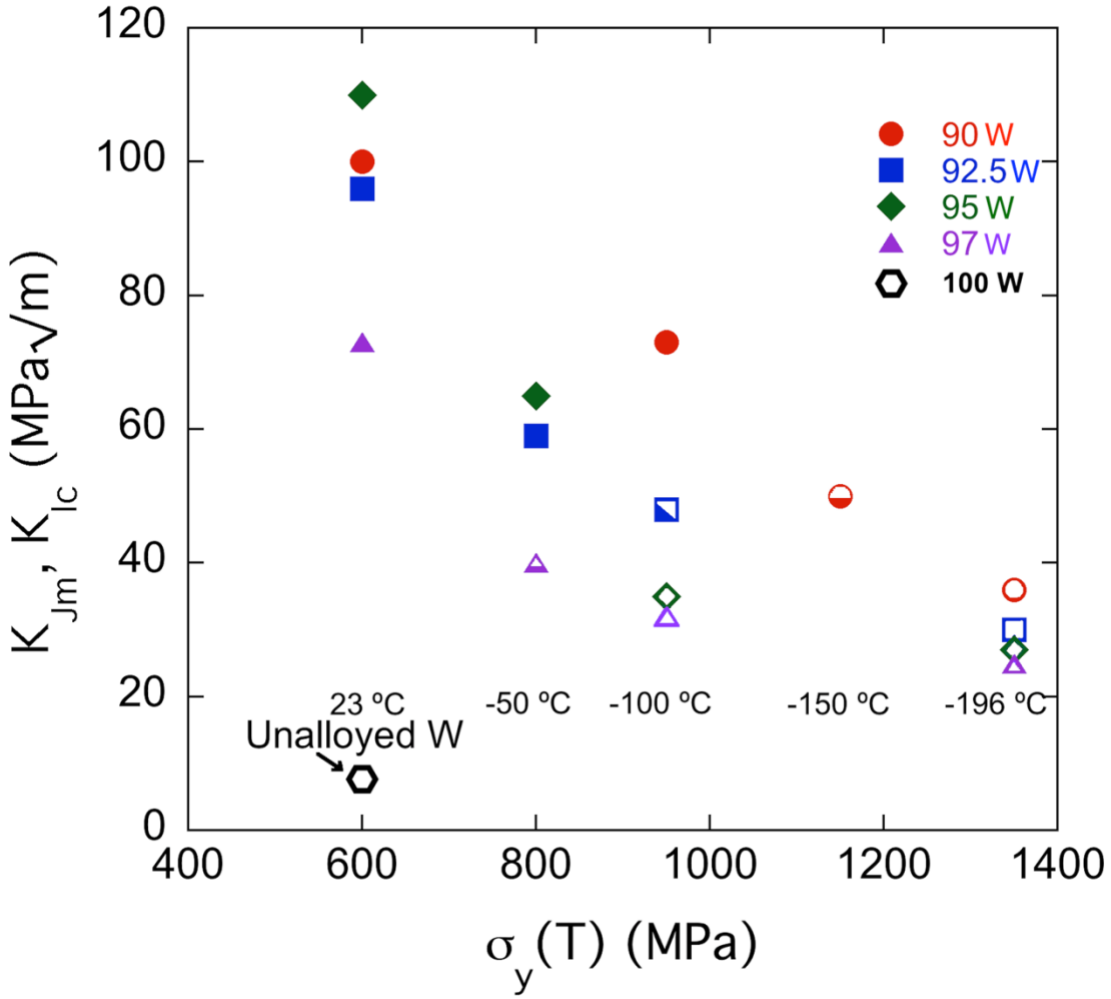

Fig. 15 Toughness (K_{Jm} or K_{Ic}) versus the estimated W yield strength (σ_y) for the various WNiFe WHAs. The filled and unfilled symbols represent stable crack growth and elastic (unstable) fracture, respectively, while the half-filled symbols represent mixed stable and unstable crack growth. The K_{Ic} for monolithic (unalloyed) W is also shown.